Dual-lidar profilers for measuring atmospheric turbulence

Maxime Thiébaut and Neil Luxcey

France Énergies Marines, Technopôle Brest-Iroise, 525 Avenue Alexis de Rochon, 29280 Plouzané, France

Correspondence: Maxime Thiébaut (maxime.thiebaut@france-energies-marines.org)

Abstract. A dual-lidar system ~~, consisting of~~ comprising two WindCube v2.1 ~~profilers with one lidar~~ Doppler lidars—one oriented horizontally at a 45~~°~~ ° angle relative to the other~~, —~~was deployed to estimate ~~along- and cross-wind variances, velocity spectra, and turbulence intensity (TI) using the "variance method"~~atmospheric turbulence using the variance method. This approach ~~computes~~ derives second-order velocity statistics directly from ~~the~~ line-of-sight (LOS) velocity variances~~to infer the full~~, enabling reconstruction of the three-dimensional velocity variance components ~~. It is benchmarked against the "traditional method "~~ without retrieving instantaneous wind vectors. Its performance is evaluated against the traditional method commonly used in the wind energy sector, which reconstructs instantaneous velocity components from single-lidar LOS measurements ~~before deriving second-order~~ prior to computing turbulence statistics. Both methods are ~~evaluated~~ assessed at a single ~~altitude~~ measurement height using a 30-day collocated dataset, with ~~reference measurements from a sonic anemometer classified~~ sonic anemometer measurements as reference and classification by atmospheric stability~~conditions. Two key performance metrics are considered:~~. The analysis focuses on turbulence intensity (TI), and performance is quantified using the mean relative bias error (MRBE) and ~~the~~ relative root mean square error (RRMSE), ~~as defined by DNV (Det Norske Veritas). Spectral analysis of the velocity components shows that , while the traditional method more closely matches the reference spectra at low frequencies, it tends to overestimate spectral energy at higher frequencies. In contrast, the variance method typically underestimates spectral energy in the~~ following DNV load-validation acceptance criteria ($|\text{MRBE}| \leq 5\%$ and RRMSE $\leq 15\%$). Results show that the variance method demonstrates improved agreement with the reference measurements across nearly all wind-speed bins. For along-wind ~~component and overestimates it in the~~ TI, MRBE values range between 0 and -5%, with RRMSE remaining below 15% over the full wind-speed range, fully satisfying the DNV criteria. For cross-wind ~~component. Furthermore, linear regression analysis reveals that the variance method captures 90-97% of the reference variances across all stability regimes~~TI, the MRBE criterion is met, while the ~~traditional method tends to overestimate—especially for~~ RRMSE threshold is exceeded. In contrast, the traditional method meets both DNV criteria for along-wind TI only at wind speeds above approximately 7 m/s and fails to satisfy either criterion for cross-wind ~~variance under unstable and neutral conditions (up to 132%)~~TI across the investigated range. Overall, the ~~variance method yields lower MRBE and RRMSE values for both along- and cross-wind TI. Specifically,~~ results demonstrate that the variance method provides more robust and DNV-compliant turbulence intensity estimates than the traditional reconstruction approach, particularly for along-wind ~~TI, MRBE decreases from 10.1% to 7.5% and RRMSE from 19.5% to 11.7%. For cross-wind TI, MRBE is reduced from up to 17.6% to 12.3%, and RRMSE from 23.4% to 18.2%.~~ turbulence relevant to wind turbine load validation.

1 Introduction

In recent years, wind lidar profiler technology has increasingly replaced traditional meteorological masts equipped with in-situ sensors such as cup or sonic anemometers for measuring key mean wind properties like speed and direction. Wind lidars can be broadly categorized based on their emission waveform ~~,~~ (pulsed or continuous~~,~~) and their associated measurement techniques. ~~Typically, pulsed lidar profilers~~ Pulsed lidar profilers commonly employ the Doppler Beam Swinging (DBS) technique (Strauch et al., 1984), ~~where the instrument samples~~ in which line-of-sight (LOS) velocities are sampled sequentially along several fixed beam directions~~, while continuous-wave lidars use the Velocity-Azimuth~~ . Velocity–Azimuth Display (VAD) ~~method (Browning and Wexler, 1968) , where LOS velocities are measured around a conical scan at a fixed elevation angle~~ scanning (Browning and Wexler, 1968) is also widely applied with pulsed lidars, as well as with continuous-wave systems, and is frequently used for turbulence retrievals (e.g., Mann et al., 2010).

Lidar profilers offer clear advantages for characterizing mean wind properties~~characterization~~, including reduced deployment costs and the ability to measure at similar or greater heights above ground compared to meteorological masts. However, wind lidar profilers have ~~yet to garner~~ not yet gained widespread acceptance for turbulence ~~measurement, which remains a focal point of ongoing~~ measurements, which remain an active area of research. In contrast to ~~turbulence data derived from~~ reference instruments such as cup or sonic anemometers, turbulence estimates from lidar profilers are ~~subject to systematic errors resulting from three primary~~ affected by systematic errors arising from three main sources: (i) inter-beam ~~effect~~effects, (ii) intra-beam averaging, and (iii) instrumental noise. ~~The inter-beam effect~~

Inter-beam effects can lead to over- or underestimation of turbulence metrics ~~due to modulation of energy from eddies of specific wavenumbers (Theriault, 1986; Gargett et al., 2009; Kelberlau and Mann, 2020). This issue is tightly linked to~~ through wavenumber-dependent modulation of turbulent energy when LOS measurements from spatially separated beams are combined (Theriault, 1986; Gargett et al., 2009; Kelberlau et al., 2020). This effect is closely linked to violations of the assumption of instantaneous spatial homogeneity ~~in~~ inherent to multi-beam techniques~~; when violated, it introduces inter-beam variance contamination~~. Intra-beam ~~effect stems from~~ effects arise from probe-volume and probe-time averaging and ~~introduces~~ lead to an underestimation of turbulent energy ~~. This bias results from two types of anisotropic filtering: (1) spatial filtering across the lidar probe volume and (2) temporal filtering due to pulse accumulation time (Thiébaut et al., 2025).~~

~~Instrumental noise contributes to turbulence overestimation by adding variance to the measured LOS velocities. For the WindCube v2.1, Thiébaut et al. (2025) found this effect to be about 5% of the total variance. Noise can be identified and removed via spectral analysis, where it appears as a flat high-frequency component (e.g., Hurther and Lemmin, 2001; Durgesh et al., 2014) , or estimated through indirect corrections. In the latter, noise variance is modeled as a function of sample volume distance from the sensors (Lhermitte and Lemmin, 1994; Zedel et al., 2002), inferred from two-point cross-correlation assuming uncorrelated noise between locations (Garbini et al., 1982), or derived from the zero-lag offset in the auto-correlation function, exploiting the lack of temporal correlation in noise (e.g., Lenschow et al., 2000).~~ due to spatial and temporal filtering of velocity fluctuations (Thiébaut et al., 2025). Instrumental noise introduces an additional variance contribution to LOS velocity measurements and can therefore bias turbulence estimates if not properly accounted for.

Turbulence intensity (TI) is a key metric in wind energy for ~~evaluating~~ assessing turbine loads, site ~~viability, and predicting~~ suitability, and energy yield. The traditional approach ~~computes~~ estimates TI from second-order statistics ~~derived from instantaneous~~ of reconstructed velocity components using LOS measurements from a single-lidar profiler. ~~However, this method combines the effects of inter- and~~ This reconstruction combines inter-beam coupling, intra-beam ~~effects~~ averaging, and instrumental noise ~~. In some cases, these biases may cancel each other out, resulting in correct~~ effects, which may partially compensate and lead to apparently accurate TI estimates for the wrong reasons (Kelberlau and Mann, 2019). ~~An alternative is to derive TI from~~

An alternative class of approaches derives turbulence statistics directly from LOS velocity variances or Doppler spectral information. Eberhard et al. (1989) showed that turbulence kinetic energy and velocity covariances can be retrieved from a full VAD scan at an elevation angle of 35.3°, provided sufficient azimuthal sampling. Later studies demonstrated that VAD-based methods can yield accurate turbulence statistics when intra-beam averaging effects are explicitly corrected (e.g., Smalikho and Banakh, 201
.

Similar concepts have been applied to pulsed Doppler lidar profilers operating in DBS configurations, where second-order ~~statistics of the three-dimensional velocity components, computed directly from the variances of the LOS velocities (Eberhard et al., 1989). Applied to a 5-beam pulsed wind lidar profiler, this method allows the estimation of five components of the Reynolds stress tensor in the instrument coordinate system. In this system, the x-axis is aligned with one pair of opposing slanted beams, and the y-axis with the other. The only component that cannot be resolved is the~~ statistics are inferred directly from LOS velocity variances. However, standard five-beam DBS geometries (one vertical and four slanted beams) cannot resolve the horizontal cross-term variance σ_{xy}~~. However, this term is essential for rotating the variances in the x and y directions to obtain the streamwise variance. In the absence of σ_{xy}, the method can be applied~~ , preventing a full rotation into the streamwise coordinate system. As a result, these approaches are generally applicable only when the ~~wind direction aligns~~ mean wind direction is aligned with a pair of ~~opposite~~ opposing slanted beams (e.g., Thiébaut et al., 2024).

~~To measure the Reynolds stress component~~ Resolving σ_{xy} ~~,~~ requires an additional slanted beam~~is required. Sathe et al. (2015) proposed such a configuration using a~~ . Sathe et al. (2015) demonstrated this using a six-beam ground-based scanning pulsed lidar ~~system called WindScanner. This device enables the computation of LOS velocity variances at five equally spaced azimuth angles on the base of a scanning cone, along with one additional measurement at the center of the scanning circle using a vertically oriented beam at the same height. The authors estimated TI by deriving~~ (WindScanner), enabling TI estimation from second-order statistics of the full three-dimensional velocity ~~components from the variances of the LOS velocities. They compared these estimates to those obtained using a continuous-wave lidar profiler based on the VAD technique and to measurements from a reference cup anemometer . The results show that, depending on atmospheric stability and the wind field component, the 6-beam method captures between 85%~~ field and validation against VAD-based lidar and ~~101% of the reference turbulence, whereas the VAD-based method captures between 66% and 87%. This indicates a significant improvement in turbulence characterization using the 6-beam approach. It is important to note that the WindScanner is not a commercial device but rather a scientific instrument used by a limited number of research groups, which constrains its broader application in operational settings. Moreover, the duration of a complete 6-beam measurement cycle with the WindScanner~~

~~was approximately 15 s, corresponding to a LOS velocity sampling rate of 0.067 Hz. Applying Taylor's frozen turbulence hypothesis, which states that eddies of size L and frequency f are advected by the mean flow velocity U, such that $f \approx U/L$, this sampling rate implies that, for a mean wind speed of 10 m/s, only eddies larger than approximately $L \approx 150$ m can be resolved. For optimized wind turbine design, however, it is essential to capture smaller turbulence structures and their associated energy content~~cup anemometer measurements. Recently, this concept has been transferred to commercial instrumentation with the release of the BEAM-6X lidar from Lumibird, inspired by the WindScanner architecture; however, as a newly introduced system, its performance and suitability for routine turbulence characterization are not yet well established.

In oceanographic studies, Acoustic Doppler Current Profilers (ADCPs) are widely used to derive first- and second-order ~~statistics of water flow . An ADCP is a~~ flow statistics. ADCPs are Doppler-based remote sensing ~~instrument that uses multiple~~ instruments that employ multiple acoustic beams to measure ~~flow~~ water velocity. A common configuration is the Janus ~~setup, as in the Workhorse Sentinel by Teledyne RDI, which features~~ geometry, exemplified by the Teledyne RDI Workhorse Sentinel, which uses four beams inclined 20° from the vertical. ~~The~~ Similar multi-beam concepts are used in atmospheric lidar systems: the WindCube v1 ~~lidar employed a similar multi-beam approach but with a steeper beam inclination. Other ADCPs,~~ employed a comparable configuration with steeper beam angles, while modern ADCPs such as the Nortek Signature series ~~,~~ use a 5-beam Janus ~~configuration~~ setup with four beams ~~slanted~~ at 25° and one vertical beam~~—closely resembling the current~~ . This closely resembles the WindCube v2.1 configuration, which combines four ~~slanted beams at $\alpha = 28°$ from the vertical~~ beams inclined at $\alpha = 28°$ with a vertical beam. ADCPs ~~can be deployed~~ may be deployed either bottom-mounted in an upward-looking configuration (e.g., Thomson et al., 2012; McMillan et al., 2016; Thiébaut et al., 2022) or ~~in a~~ downward-looking ~~configuration~~ when installed on ~~a floating structure or towed by~~ floating platforms or vessels (e.g., Goddijn-Murphy et al., 2013; Sentchev et al., 2019; Thiébaut et al., 2019).

The method ~~that uses~~ based on second-order statistics of LOS velocity ~~to reconstruct the variance of~~ measurements to reconstruct three-dimensional velocity ~~components can also be applied to ADCP measurements. In ocean sciences, this approach is~~ variances is well established in oceanography and is commonly referred to as the variance method ~~(e.g., Stacey et al., 1999a; Lu and Luec~~ (e.g., Stacey et al., 1999a; Lu and Lueck, 1999; Rippeth et al., 2002). Turbulence analysis using a ~~single-ADCP~~ single ADCP (up to five beams) typically relies on assumed turbulence anisotropy ratios, often derived from laboratory ~~studies (e.g., Stacey et al., 1999b;~~ experiments (e.g., Stacey et al., 1999b; Lueck et al., 2002; Peters and Johns, 2006). However, ~~Burchard et al. (2008) argue that this approach is problematic, as~~ such assumptions can introduce substantial uncertainty. Burchard et al. (2008) demonstrated that the difference between ~~fully anisotropic and isotropic turbulence can lead to~~ isotropic and fully anisotropic turbulence may lead to up to a six-fold ~~discrepancy in estimated~~ error in turbulent kinetic energy (TKE) ~~using a Teledyne RDI~~ estimates from a four-beam ADCP. These assumptions are ~~necessary because it is not possible to resolve all six independent~~ unavoidable because fewer than six independent beams cannot resolve all components of the Reynolds stress tensor~~with fewer than six beams~~.

To ~~overcome~~ address this limitation, Vermeulen et al. (2011) proposed a dual-ADCP ~~setup using two 4-beam~~ configuration combining two four-beam RDI instruments with ~~slanted beams. The second ADCP was oriented horizontally with~~ a 45° ~~heading offset relative to the first~~relative heading offset, forming an ~~8-beam configuration. This specific~~ eight-beam system.

This orientation was shown numerically to minimize ~~error in velocity variance estimates. Additionally, the second ADCP was pitched at~~ variance-estimation errors. One instrument was additionally pitched by 20°~~to align~~, aligning one beam vertically ~~upward,~~ and enabling direct measurement of the vertical velocity component. With eight independent beams, ~~assumptions about anisotropy become unnecessary, and~~ the full Reynolds stress tensor can be resolved without invoking anisotropy assumptions and rotated into any desired coordinate frame. This ~~configuration~~ approach was later implemented by Thiébaut et al. (2020) to investigate the ~~TKE~~ turbulent kinetic energy budget in the ~~highly energetic Alderney Race (France). Mercier et al. (2021) further validated the method by replicating the 8-beam setup in~~ Alderney Race tidal channel and was further validated using large-eddy simulations by Mercier et al. (2021).

Building on the methodology introduced by Vermeulen et al. (2011) for ADCPs, we developed a modified version tailored to dual-WindCube v2.1 lidar profilers. This configuration provides the minimum number of independent beams required by the variance method using well-established commercial lidar profilers, as an alternative to recently commercialized six-beam lidar profilers, such as the Beam6X WindPower developed by Lumibird, which are inspired by the WindScanner concept. The ~~dual-lidar system is used to estimate along- and cross-wind variances, velocity spectra, and TI using the variance method. This~~ method is benchmarked against the traditional ~~method~~ approach used in the wind power industry. Both methods are evaluated at a single altitude using a 30-day collocated dataset, with reference measurements from a 3D sonic anemometer classified by atmospheric stability conditions. Two key performance metrics are considered: the mean relative bias error (MRBE) and the relative root mean square error (RRMSE), as defined by DNV (Det Norske Veritas) (DNV, 2023).

The remainder of this paper is organized as follows. The study begins with a description of the study site (Sect. 2.1), instrumentation (Sect. 2.2), and data selection (Sect. 2.3), along with methods for instrumental noise correction and spike filtering (Sects. 2.4 and 2.5). This section also presents the traditional method for single-lidar profilers, the variance method for dual-lidar profilers, and the reference sonic anemometer measurements used to derive ~~velocity variances,~~ TI (Sect. 2.6) ~~, and velocity power spectral density~~ and velocity spectra (Sect. 2.7). Atmospheric stability classification based on the sonic anemometer measurements is described in Sect. 2.8. Error metrics for method evaluation are defined in Sect. 2.9. The results of the comparative analysis between the variance and traditional methods are presented in Sect. 3, followed by a discussion in Sect. 4. Finally, Sect. 5 summarizes the main findings and provides concluding remarks.

2 Data and methods

2.1 Study site and meteorological mast

The measurement mast ~~has been installed since February 2015, located~~ is located approximately 13 km offshore from Fécamp, along the coast of Normandy, France (Fig. 1). ~~Initially operated by EDF (Électricité de France), the operation of the mast was transferred to France~~ It was originally installed for wind farm site characterization and is now operated by France Énergies Marines~~at the end of 2022. The entire structure, including the foundation and measurement equipment, stands 90 m tall. The lattice tower, which supports various sensors, reaches a height of 40 m, while the top of the mast rises approximately 60 m above sea level, depending on tidal variations. The average tidal range at the site is 8.8 m. The mast is anchored to a reinforced~~

~~concrete structure, resembling gravity-based foundations, with a diameter of 23 mand~~. The mast is situated within the offshore wind farm area, with the nearest turbine located approximately 400 m to the west. The site is characterized by strong tidal conditions, with a ~~total weight of 1,800 tons, placed directly on the seabed.~~ mean tidal range of about 8.8 m, and represents a typical offshore environment for wind energy applications. Fig. 2 summarizes the mean wind conditions observed during the 30-day analysis period. The mean wind speed was 8.5 m/s, with a maximum observed value of 21.0 m/s. The wind direction distribution is dominated by south-westerly flows, with a mean wind direction of approximately 205° and a directional spread of about 74°. These conditions are representative of an offshore wind regime and provide a broad range of wind speeds and directions for the evaluation of the lidar-based turbulence retrieval methods.

~~The mast was initially constructed to characterize the site for the wind farm deployment, providing essential data for the planning and design phases, and to test the foundation, which could potentially be used for the wind turbine foundations. It is positioned in front of the first row of wind turbines to the south of the wind farm, with the nearest turbine located 400 mto the west. The 497-megawatt (MW) wind project, which began operating in May 2024, comprises 71 Siemens Gamesa Renewable Energy 7-MW turbines. These turbines are located between 13 and 24 km off the coast of Fécamp, at depths of approximately 30 m (Fig. 1b). The turbines span an area of about 60 km^2.~~

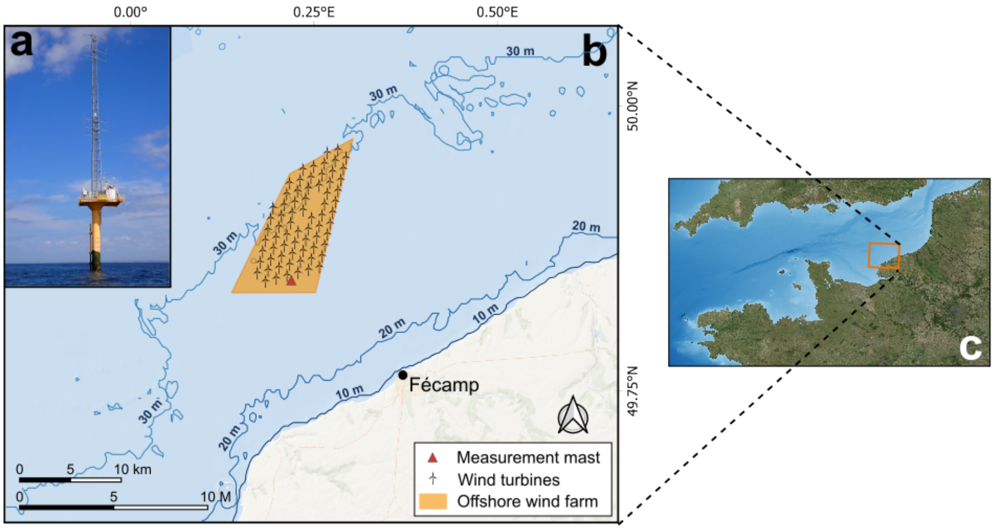

Figure 1. Photograph of the measurement mast (a), located 13 km off the coast of Fécamp, situated in front of the first row of wind turbines in the offshore wind farm (b), which is deployed off the coast of Normandy, France (c).

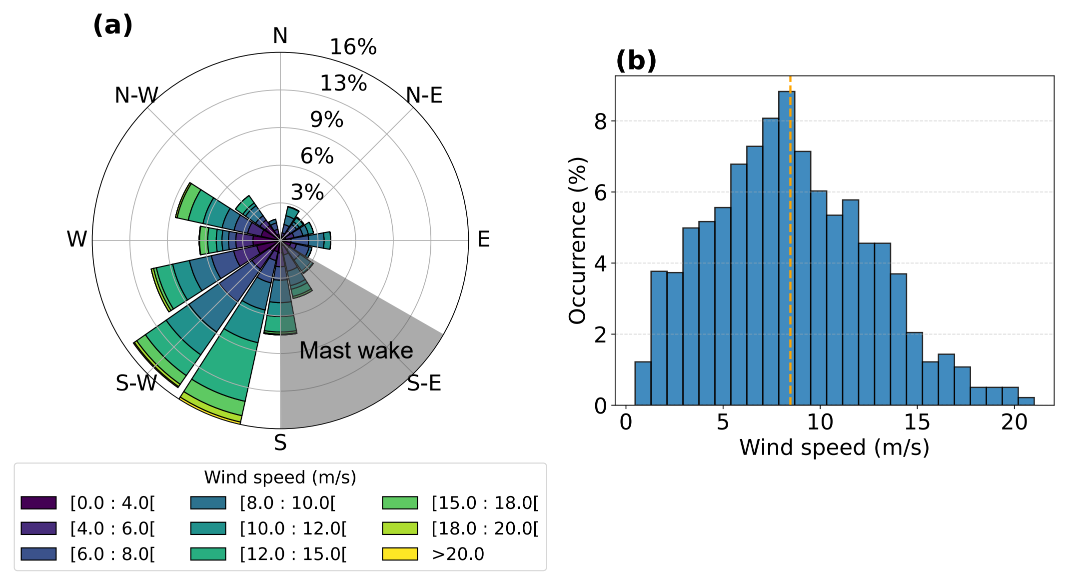

Figure 2. (a) Wind rose for the analysis period. The grey shaded sector indicates wind directions affected by mast wake and excluded from the analysis. (b) Histogram of wind speed occurrence. The vertical orange line indicates the mean wind speed.

2.2 Sensors equipment

The measurement mast is equipped with a 3D THIES sonic anemometer mounted on a boom at a height of 39 m above the platform (Fig. 3a). The measurement volume of the sonic anemometer is positionned at 39.5 m, as it is located 0.5 m from the tip of the boom. The boom is oriented at an angle of -60° from True North (Fig. 3b). The anemometer is aligned such that the x-axis points toward True North, the y-axis toward the West, and the z-axis vertically upward. The (x, y, z) coordinate system associated with the sonic anemometer served as the reference coordinate system in this study. The anemometer collects wind velocity data at an acquisition rate of 10 Hz.

To complement this setup, two Vaisala offshore WindCube v2.1 lidar profilers were installed at the platform level (Fig. 3b and Fig. 4bc). The primary lidar, referred to as lidar A, was oriented such that beams 1 and 3—aligned with the x-axis of the instrument's coordinate system—were directed toward True North, while beams 2 and 4 were aligned with the y-axis. The fifth beam of lidar A pointed vertically along the z-axis. Note that the manufacturer configured the z-axis of the lidar to point vertically downward. The secondary lidar, referred to as lidar B, was mounted adjacent to lidar A and rotated at $\theta = 45°$ in the horizontal plane relative to lidar A. Both lidars were installed with a tilt angle of less than 0.2°. Together, the two lidars formed a combined 10-beam scanning arrangement (Fig. 4a), enabling measurements of LOS velocities at ten vertical levels ranging from 40 m to 240 m above the platform. LOS velocity data were recorded at a sampling rate of 0.25 Hz. ~~To enable a consistent~~ For consistency in the point-by-point comparison, the sonic anemometer ~~dataset was downsampled~~ time series was resampled to the same rate ~~. This step is critical for ensuring that all measurements are temporally aligned and comparable.~~

~~The downsampling was performed using a decimation approach, which reduces the number of data points by an integer factor while applying a low-pass filter. This effectively reproduces what a device operating at the lower sampling rate would measure, capturing the energy of larger eddies but necessarily filtering out smaller, high-frequency turbulent fluctuations that cannot be resolved at the lower rate.~~ using a standard decimation procedure.

Additionally, atmospheric data are collected by a Vaisala WXT 530 weather transmitter, installed on the mast at a height of 39 m above the platform. This sensor provides 10-min averaged values of pressure, temperature, and humidity.

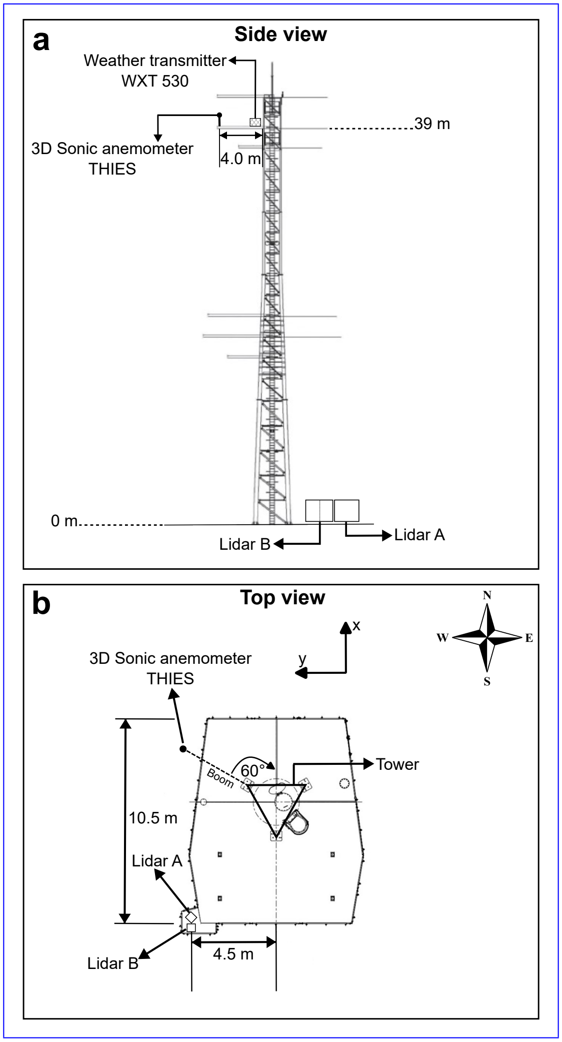

Figure 3. Side view (a) and top view (b) schematics of the 40-m measurement mast, detailing the deployed sensors and their positions on the mast and platform.

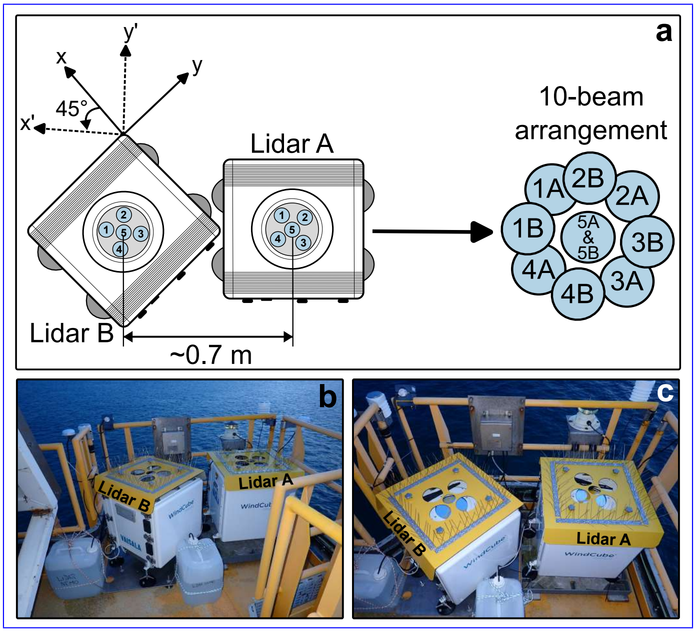

Figure 4. (a) Schematic of the 10-beam arrangement formed by combining the five beams of lidar A with the five beams of lidar B, which is rotated 45° relative to lidar A. (b) Side view and (c) top view photographs of the setup installed at the platform level.

2.3 Data selection

A 30-day dataset spanning from April 1 to May 1, 2024, was compiled for turbulence analysis. This dataset was divided into 1,440 non-overlapping 30-min ensembles. The choice of a 30-min averaging window~~—~~, rather than the ~~traditional~~ 10-min interval commonly used in ~~the wind energy industry—was motivated by the goal of reducing~~ wind energy practice and in DNV error metrics, was made deliberately to reduce random errors in turbulence ~~measurements, in accordance with the recommendations of Lenschow et al. (1994)~~statistics. Longer averaging periods improve statistical convergence of second-order moments, as discussed by Lenschow et al. (1994), and are therefore better suited for the present turbulence analysis. The analysis focused on wind speeds exceeding 3 m/s, corresponding to the typical cut-in speed of most wind turbines. Applying this threshold led to the exclusion of approximately 6% of the original dataset. Additionally, wind measurements associated with wind directions between 120° and 180° (relative to True North) were excluded to avoid contamination from mast wake effects affecting the sonic anemometer data ~~.~~ (Fig. 2a). This directional filtering removed a further 11% of the remaining ensembles. To ensure data quality, any 30-min ensemble containing less than 90% valid velocity measurements was also discarded, resulting in an additional 9% reduction. Individual velocity measurements were considered valid only if their carrier-to-noise ratio (CNR), provided by the lidar systems, was greater than -23 dB, as recommended by the manufacturer. After applying all filtering criteria, a total of N = 1,098 30-min ensembles were retained for turbulence analysis. ~~The final dataset spans wind speeds ranging from 3 to 21 m/s, with a mean wind speed of 9.7 m/s and a median of 9.3 m/s.~~

2.4 Instrumental noise

Lidar measurements are inherently influenced by signal noise and ~~potential~~ by small variations in aerosol ~~fall speeds, both of which~~gravitational settling velocities, which—although weak—can contribute additional terms to the observed variance. Assuming that all atmospheric flow contributions to the observed LOS velocity variance within the considered short timescales are of a turbulent nature, the variance $\sigma_{b_i}^2$ of the LOS velocity measured by beam i, can be expressed as the sum of three independent terms (Doviak and Zrnic, 1993):

$$\sigma_{b_i}^2 = \sigma_{p_i}^2 + \sigma_{n_i}^2 + \sigma_{d_i}^2 \tag{1}$$

Here, $\sigma_{p_i}^2$ represents the net contribution from atmospheric turbulence at scales measurable by the lidar (Brugger et al., 2016), $\sigma_{n_i}^2$ denotes the variance associated with instrumental noise, and $\sigma_{d_i}^2$ accounts for the variance caused by variations in aerosol terminal fall speeds within the probe volume. However, $\sigma_{d_i}^2$ can typically be neglected, as particle fall speeds are generally less than 1 cm/s (e.g., Bodini et al., 2018).

The noise contribution $\sigma_{n_i}^2$ is often quantified through an autocorrelation approach. In this method, the temporal autocorrelation function of the measured LOS velocity time series,

$$R(\tau) = \frac{\langle b_i(t)\, b_i(t+\tau)\rangle}{\sigma_{b_i}^2}, \tag{2}$$

is examined at short time lags τ. While atmospheric fluctuations remain correlated over small τ, the noise component is uncorrelated and manifests as a discontinuity at the first nonzero lag. The reduction of $R(\tau)$ between $\tau = 0$ and $\tau = \Delta t$ can therefore be used to estimate $\sigma_{n_i}^2$ ~~(e.g., Lenschow et al., 2000)~~(e.g., Mayor et al., 1997; Lenschow et al., 2000). For a wind lidar profiler such as the WindCube v2.1, the sampling interval Δt corresponds to the accumulation time of the Doppler signal at one LOS position. This separation enables the retrieval of the turbulence-related variance $\sigma_{p_i}^2$ with reduced contamination from instrumental effects. Note that, for consistency, instrumental noise were similarly removed from variance of the time series of the instantaneous reconstructed horizontal velocities, u_x and u_y, employed in the traditional method (Sect. 2.6.2).

2.5 Spike filtering

To remove spurious outliers in the velocity measurements, a ~~spike filtering~~ spike-filtering procedure following Wang et al. (2015) was applied. ~~This method is designed to identify unrealistic spikes in wind signal records that may arise from intermittent low signal-to-noise ratios or other measurement artifacts. The filter operates on the time series by evaluating the deviation of each data point from the local median within a moving window. If the deviation exceeds a specified threshold, typically defined in terms of multiples of the local standard deviation, the point is flagged as a spike and subsequently removed or replaced through interpolation. In the present study, this filtering technique~~ The method was implemented over consecutive 30-min windows and is based on the analysis of differences between adjacent velocity samples. A data point was flagged as a spike when the absolute differences at two consecutive time steps exceeded twice the interquartile range (IQR) of the local difference distribution and exhibited opposite signs. Identified spikes were removed by setting the corresponding values to

NaN (Not a Number). This filtering was applied consistently ~~across~~ to all datasets, including ~~the LOS velocity time series from the lidar profilers, the~~ lidar LOS velocities, reconstructed horizontal wind components~~u_x~~ , and ~~u_y from the lidar, and the three-dimensional velocity components measured by the sonic anemometer . This ensures that spurious outliers are removed from both remote sensing and in situ measurements, thereby improving the robustness of the turbulence statistics derived from these observations~~sonic anemometer measurements.

2.6 Reconstruction of turbulence metrics

2.6.1 Sonic anemometer

To reduce the influence of alignment and tilt errors~~on the variance estimates, a two-step coordinate rotation is applied to~~ , the sonic anemometer data ~~(Foken and Mauder, 2008). Following the procedure described by Kaimal and Finnigan (1994)~~ were processed using a standard double-rotation procedure (Kaimal and Finnigan, 1994; Foken and Mauder, 2008). First, the coordinate system ~~of the sonic anemometer (x, y, z) is first rotated such that the mean velocity component $< u_y >$—where the brackets denote a temporal average over a 30-min period—becomes zero, and the u_x component aligns~~ was rotated in the horizontal plane to align the streamwise velocity component with the mean wind direction ~~Θ defined as:~~

~~$\Theta = \arctan\left(\frac{< u_y >}{< u_x >}\right)$~~

~~This rotation yields a new intermediate coordinate system (x_1, y_1, z_1), with transformed velocity components given by:~~

~~$u_{x_1} = u_x \cos\Theta + u_y \sin\Theta$~~

~~$u_{y_1} = -u_x \sin\Theta + u_y \cos\Theta$~~

~~$u_{z_1} = u_z$~~

~~In the second rotation , the intermediate coordinate system (x_1, y_1, z_1) is further rotated~~ over each 30-min averaging period. A second rotation in the vertical plane ~~by an angle:~~

~~$\phi = \arctan\left(\frac{< u_{z_1} >}{< u_{x_1} >}\right)$~~

~~resulting in a final coordinate system (x_2, y_2, z_2), in which the~~ was then applied to ensure zero mean vertical velocity~~component is zero. The velocity components in this new system are given by:~~

~~$u_{x_2} = u_{x_1} \cos\phi + u_{z_1} \sin\phi$~~

~~$u_{y_2} = u_{y_1}$~~

~~$u_{z_2} = -u_{x_1} \sin\phi + u_{z_1} \cos\phi$~~

~~In this final rotated frame~~. In the resulting coordinate system, the velocity components are denoted as ~~$u = u_{x_2}$, $v = u_{y_2}$ and $w = u_{z_2}$~~u, v, and w, corresponding to the along-wind, cross-wind~~and vertical-wind~~ , and vertical components, respectively.

~~These components are then used to compute the reference along~~ The along- and cross-wind ~~variances—σ_u^2 and σ_v^2—employed to derive the reference along and cross-wind turbulence intensity—TI_u and TI_v—defined as:~~

~~$\mathrm{TI}_u = \frac{\sqrt{\sigma_u^2}}{U}$~~

turbulence intensities, TI_u and TI_v were computed as:

$$\mathrm{TI}_u = \frac{\sigma_u}{U}, \tag{3}$$

$$\mathrm{TI}_v = \frac{\sigma_v}{U}. \tag{4}$$

~~$\mathrm{TI}_v = \frac{\sqrt{\sigma_v^2}}{U}$~~

~~where $U = \sqrt{\langle u\rangle^2 + \langle v\rangle^2}$~~

where σ_u and σ_v are the standard deviations of u and v, and $U = \langle\sqrt{u^2+v^2}\rangle$ is the mean ~~wind speed~~horizontal wind speed, where the angle brackets $\langle\cdot\rangle$ denote temporal averaging.

2.6.2 Single-lidar profiler — Traditional method

~~The traditional method for deriving turbulence information from lidar profiler measurements involves computing second-order statistics from reconstructed instantaneous velocity components, which are inferred from LOS velocities measured by~~

For the traditional lidar-based approach, instantaneous horizontal velocity components were reconstructed from LOS measurements of a single-lidar profiler. ~~Similarly to the sonic anemometer dataset, the reconstructed instantaneous horizontal velocities u_x and u_y from the lidar~~ The reconstructed velocities were rotated in the horizontal plane ~~to obtain (u_{x_1}, u_{y_1}) using Eq. **??** and **??**. A second rotation was not required due~~ following the same procedure as for the sonic anemometer. Due to the small ~~tilt angle of the lidars. Therefore, after the first rotation , the lidar velocities can be expressed as $u = u_{x_1}$ and $v = u_{y_1}$. These components are then~~ lidar tilt angles, no additional vertical rotation was applied. The resulting velocity components were used to compute the ~~variances $\tilde{\sigma}_u^2$ and $\tilde{\sigma}_v^2$. The tilde notation is used here to denote turbulence metrics derived using the traditional method. The along and cross-wind turbulence intensity—$\tilde{\mathrm{TI}}_u$ and $\tilde{\mathrm{TI}}_v$—derived from this method are then defined as:~~

~~$\tilde{\mathrm{TI}}_u = \frac{\sqrt{\tilde{\sigma}_u^2}}{U}$~~

~~$\tilde{\mathrm{TI}}_v = \frac{\sqrt{\tilde{\sigma}_v^2}}{U}$~~

standard deviations $\tilde{\sigma}_u$ and $\tilde{\sigma}_v$, from which the corresponding turbulence intensities, denoted as $\tilde{\mathrm{TI}}_u$ and $\tilde{\mathrm{TI}}_v$, were derived following the definition given in Sect. 2.6.1.

2.6.3 Dual-lidar profilers — Variance method

The variance method involves the computation of second-order statistics of the three-dimensional velocity components from the LOS velocity variances. Building on the methodology introduced by Vermeulen et al. (2011) for ADCPs, we developed a modified version tailored to dual-WindCube v2.1 lidar profilers, each with a 5-beam configuration. Our approach constructs a ten-element vector $\boldsymbol{b}$ containing noise-corrected LOS variances, $\sigma^2_{p_i}$, from both devices, allowing reconstruction of the full Reynolds stress tensor. The vector is defined as:

$$\boldsymbol{b} = \left[\sigma^2_{p_1,\mathrm{A}}, \sigma^2_{p_2,\mathrm{A}}, \sigma^2_{p_3,\mathrm{A}}, \sigma^2_{p_4,\mathrm{A}}, \sigma^2_{p_5,\mathrm{A}}, \sigma^2_{p_1,\mathrm{B}}, \sigma^2_{p_2,\mathrm{B}}, \sigma^2_{p_3,\mathrm{B}}, \sigma^2_{p_4,\mathrm{B}}, \sigma^2_{p_5,\mathrm{B}}\right] \tag{5}$$

where subscripts p_1 to p_5 denote the five individual beam of each lidar profiler, and the ~~superscripts~~ subscripts A and B refer to the primary and secondary lidar profilers, respectively. ~~In Eq. 5, $\sigma^2_{p_i,\mathrm{A}}$ and $\sigma^2_{p_i,\mathrm{B}}$ are given by:~~

$$\sigma^2_{p_i,\mathrm{A}} = \int\limits_0^\infty S_{i,\mathrm{A}}(f)df$$

$$\sigma^2_{p_i,\mathrm{B}} = \int\limits_0^\infty S_{i,\mathrm{B}}(f)df$$

~~where $S_{i,\mathrm{A}}$ and $S_{i,\mathrm{B}}$ are the LOS velocity power spectral density measured by beam i of lidars A and B.~~

A transformation matrix ~~T is then~~ $\mathbf{T} \in \mathbb{R}^{10\times 3}$ is defined to project the LOS velocity variances into the reference coordinate system ~~(x, y, z). This~~ (x, y, z). The matrix consists of two components: one associated with the beam geometry of the primary lidar, and ~~the other corresponding to the~~ one associated with the secondary lidar. The latter includes a counterclockwise rotation ~~matrix~~ to account for the relative yaw angle θ between the two devices. The ~~full~~ transformation matrix is expressed as:

$$\mathbf{T} = \begin{pmatrix} \sin\alpha & 0 & -\cos\alpha \\ 0 & \sin\alpha & -\cos\alpha \\ -\sin\alpha & 0 & -\cos\alpha \\ 0 & -\sin\alpha & -\cos\alpha \\ 0 & 0 & -1 \\ 0 & 0 & 0 \\ 0 & 0 & 0 \\ 0 & 0 & 0 \\ 0 & 0 & 0 \\ 0 & 0 & 0 \end{pmatrix} + \begin{pmatrix} 0 & 0 & 0 \\ 0 & 0 & 0 \\ 0 & 0 & 0 \\ 0 & 0 & 0 \\ 0 & 0 & 0 \\ \sin\alpha & 0 & -\cos\alpha \\ 0 & \sin\alpha & -\cos\alpha \\ -\sin\alpha & 0 & -\cos\alpha \\ 0 & -\sin\alpha & -\cos\alpha \\ 0 & 0 & -1 \end{pmatrix} \begin{pmatrix} \cos\theta & -\sin\theta & 0 \\ \sin\theta & \cos\theta & 0 \\ 0 & 0 & 1 \end{pmatrix}. \tag{6}$$

As a reminder $\alpha = 28°$ is the zenith angle and $\theta = 45°$ corresponds to the angle of rotation in the horizontal plane of lidar B relative to lidar A.

To extract the Reynolds stress tensor components from the LOS ~~variances, an intermediate 10×6 matrix $\mathbf{Q}$ is computed, with elements defined as:~~ velocity variances, a 10×6 matrix $\mathbf{Q}$ is constructed from $\mathbf{T}$. Each row of $\mathbf{Q}$ is formed from quadratic combinations of the corresponding row of $\mathbf{T}$ as:

~~$\mathbf{Q}$~~ $Q_p =$ ~~$T_{p,q} \cdot T_{p,m}$~~ $\begin{pmatrix} T_{p,1}^2 & T_{p,2}^2 & T_{p,3}^2 & 2T_{p,1}T_{p,2} & 2T_{p,1}T_{p,3} & 2T_{p,2}T_{p,3} \end{pmatrix},$ (7)

where ~~$p = 1, \ldots, 10$ corresponds to the ten beams in the dual-lidar configuration, with beams 1 to 5 (denoted 1A, 2A, 3A, 4A and 5A in Fig. 4a) from the primary lidar and beams 6 to 10 (denoted 1B, 2B, 3B, 4B and 5B in Fig. 4a) from the secondary lidar, and $q, m = 1, 2, 3$ correspond to the three spatial directions in the reference coordinates system. The matrix,~~ $p = 1, \ldots, 10$ denotes the beam index and $T_{p,q}$ is the element of $\mathbf{T}$ associated with beam p and spatial direction q.

The matrix $\mathbf{Q}$ ~~,~~relates the LOS variance vector ~~$\boldsymbol{b}$~~ $\boldsymbol{b}$ to the Reynolds stress vector ~~$\boldsymbol{r}$ as:~~ $\boldsymbol{r}$ as:

$$\boldsymbol{b} = \mathbf{Q}\,\boldsymbol{r}, \tag{8}$$

which is equivalent, for each beam p, to:

$$b_p = \sum_{q=1}^{3} \sum_{m=1}^{3} T_{p,q} T_{p,m} r_{qm}. \tag{9}$$

Eq. ~~??~~ 8 is overdetermined and is solved in a least-squares sense using the Moore–Penrose pseudoinverse:

$$\boldsymbol{r} = \left(\mathbf{Q}^\top \mathbf{Q}\right)^{-1} \mathbf{Q}^\top \boldsymbol{b} = \mathbf{Q}^{+} \boldsymbol{b} \tag{10}$$

Accuracy can be optimized by maximizing the determinant of $\mathbf{Q}^\top\mathbf{Q}$; if this determinant approaches zero, the solution becomes ill-conditioned. In our case, since each lidar provides a spatially uniform distribution of beams, the only design variable that influences the determinant is the relative orientation between sensors. By offsetting lidar B by 45°, we maximize the angular spread of the combined sensing directions, thereby maximizing $\det(\mathbf{Q}^\top\mathbf{Q})$ and improving the conditioning of the solution.

The six-element vector $\boldsymbol{r}$ contains the independent components of the Reynolds stress tensor, $\mathbf{R}$, which is reconstructed as a symmetric 3×3 matrix:

$$\mathbf{R} = \begin{pmatrix} r_1 & r_4 & r_5 \\ r_4 & r_2 & r_6 \\ r_5 & r_6 & r_3 \end{pmatrix} = \begin{pmatrix} \hat{\sigma}_x^2 & \hat{\sigma}_{xy} & \hat{\sigma}_{xz} \\ \hat{\sigma}_{xy} & \hat{\sigma}_y^2 & \hat{\sigma}_{yz} \\ \hat{\sigma}_{xz} & \hat{\sigma}_{yz} & \hat{\sigma}_z^2 \end{pmatrix} \tag{11}$$

The hat notation is used here to denote turbulence metrics derived using the variance method.

The Reynolds stress tensor is subjected to the same initial coordinate rotation described in Sect. 2.6.1, resulting in transformed components within the rotated horizontal coordinate system (x_1, y_1). In this frame, the variances of the along-wind and cross-wind velocity components—denoted $\hat{\sigma}_u^2 = \hat{\sigma}_{x_1}^2$ and $\hat{\sigma}_v^2 = \hat{\sigma}_{y_1}^2$, respectively—are given by ~~:~~

$$\hat{\sigma}_u^2 = \hat{\sigma}_x^2 \cos^2\Theta + \hat{\sigma}_y^2 \sin^2\Theta + \hat{\sigma}_{xy} \sin(2\Theta), \tag{12}$$

$$\hat{\sigma}_v^2 = \hat{\sigma}_x^2 \sin^2\Theta + \hat{\sigma}_y^2 \cos^2\Theta - \hat{\sigma}_{xy} \sin(2\Theta). \tag{13}$$

The corresponding along- and cross-wind turbulence intensities, denoted $\hat{\mathrm{TI}}_u$ and $\hat{\mathrm{TI}}_v$, ~~obtained from the variance method, are then defined as:~~

~~$\hat{\mathrm{TI}}_u = \frac{\sqrt{\hat{\sigma}_u^2}}{U}$~~

~~$\hat{\mathrm{TI}}_v = \frac{\sqrt{\hat{\sigma}_v^2}}{U}$~~

are then obtained from these variances following the definition given in Sect. 2.6.1.

2.7 Velocity spectra

~~The velocity power spectral density, hereafter referred to as the velocity spectra ,~~ Velocity spectra provides valuable insight into the distribution of turbulent kinetic energy across different scales of motion within the wind flow. This information is essential for characterizing turbulence and understanding its impact on wind turbine performance and structural loading.

Velocity spectra were estimated using Welch's method (Welch, 1967), which involves segmenting the time series into overlapping windows, applying a windowing function, computing a periodogram for each segment, and averaging the resulting periodograms to obtain a stable spectral estimate. A Hann window with 50% overlap was used to reduce spectral leakage and improve frequency resolution.

The analysis focused on the along-wind and cross-wind velocity components, derived from time series of the horizontal wind speeds u and v, respectively, as measured by the sonic anemometer. These were used to compute the spectra S_{uu} and S_{vv}.

For lidar measurements, two methods were employed to estimate the velocity spectra:

1. **Traditional method** – Spectra were computed directly from the along-wind and cross-wind velocities, obtained by rotating the instantaneous velocities u_x and u_y. This yielded spectral estimates $\tilde{S}_{uu}$ and $\tilde{S}_{vv}$.
2. **Variance method** – Spectra were computed from the LOS velocity spectra associated with each beam in the 10-beam configuration. These LOS spectra were assembled into the vector $\boldsymbol{\beta}$:

$$\boldsymbol{\beta} = [S_{1,\mathrm{A}}, S_{2,\mathrm{A}}, S_{3,\mathrm{A}}, S_{4,\mathrm{A}}, S_{5,\mathrm{A}}, S_{1,\mathrm{B}}, S_{2,\mathrm{B}}, S_{3,\mathrm{B}}, S_{4,\mathrm{B}}, S_{5,\mathrm{B}}] \tag{14}$$

The matrix $\mathbf{Q}^{+}$, defined in Eq. 10, was then used to compute the vector of spectral components:

$$\boldsymbol{s} = \mathbf{Q}^{+}\boldsymbol{\beta} \tag{15}$$

The resulting six-element vector $\boldsymbol{s}$ contains the spectral components associated with the independent elements of the symmetric velocity spectral tensor $\mathbf{S}$, which is reconstructed as:

$$\mathbf{S} = \begin{pmatrix} s_1 & s_4 & s_5 \\ s_4 & s_2 & s_6 \\ s_5 & s_6 & s_3 \end{pmatrix} = \begin{pmatrix} \hat{S}_{xx} & \hat{S}_{xy} & \hat{S}_{xz} \\ \hat{S}_{xy} & \hat{S}_{yy} & \hat{S}_{yz} \\ \hat{S}_{xz} & \hat{S}_{yz} & \hat{S}_{zz} \end{pmatrix} \tag{16}$$

Table 1. Classification of atmospheric stability based on Monin–Obukhov length.

Stability conditions	L_{MO} [m]
Unstable	-500 $\leq L_{\mathrm{MO}} \leq$ -50
Neutral	$\lvert L_{\mathrm{MO}} \rvert \geq$ 500
Stable	50 $\leq L_{\mathrm{MO}} \leq$ 500

The along-wind and cross-wind velocity spectra, $\hat{S}_{uu}$ and $\hat{S}_{vv}$, were then obtained via coordinate transformation:

$$\hat{S}_{uu} = \hat{S}_{xx}\cos^2\Theta + \hat{S}_{yy}\sin^2\Theta + \hat{S}_{xy}\sin(2\Theta) \tag{17}$$

$$\hat{S}_{vv} = \hat{S}_{xx}\sin^2\Theta + \hat{S}_{yy}\cos^2\Theta - \hat{S}_{xy}\sin(2\Theta) \tag{18}$$

For ~~simplicity~~conciseness, the along-wind spectra S_{uu}, $\tilde{S}_{uu}$, and $\hat{S}_{uu}$, and cross-wind spectra S_{vv}, $\tilde{S}_{vv}$, and $\hat{S}_{vv}$, are hereafter referred to as S_u, $\tilde{S}_u$, and $\hat{S}_u$, and S_v, $\tilde{S}_v$, and $\hat{S}_v$, respectively~~, for conciseness~~.

2.8 Atmospheric stability

The 30-min subsets were classified into different atmospheric stability regimes based on the Monin–Obukhov length, L_{MO}, using the thresholds listed in Table 1 (Sathe et al., 2011). The Monin–Obukhov length was estimated via the eddy covariance method (Kaimal and Finnigan, 1994) using 10 Hz measurements from the 3D sonic anemometer. The 30-min virtual potential temperature, θ_{v}, was computed by aggregating 10-min averaged temperature measurements from the WXT 530 sensor. L_{MO} is defined as:

$$L_{\mathrm{MO}} = -\frac{u_*^3\theta_{\mathrm{v}}}{\kappa g \sigma_{w\theta_{\mathrm{v}}}}\frac{u_*^3\theta_{\mathrm{v}}}{\kappa g \sigma_{w\theta_{\mathrm{s}}}} \tag{19}$$

where $\kappa = 0.4$ is the von Kármán constant, g is the acceleration due to gravity, θ_{v} is the 30-min mean virtual potential temperature ~~, and $\sigma_{w\theta_{\mathrm{v}}}$~~ derived from the WXT530, and $\sigma_{w\theta_s}$ is the covariance between the vertical wind speed w and ~~θ_{v}~~the sonic temperature θ_s, representing the ~~virtual~~ kinematic heat flux. The friction velocity, u_*, is computed from the turbulent momentum fluxes as:

$$u_* = \left(\sigma_{uw}^2 + \sigma_{vw}^2\right)^{1/4} \tag{20}$$

where σ_{uw} and σ_{vw} are the covariances between the horizontal velocity components (u and v) and the vertical velocity component w, respectively. Among the 1,098 30-min subsets, 37.1% were recorded under neutral conditions, 20.5% under stable conditions, and 42.4% under unstable conditions. Unless otherwise stated, the results presented in this work are based on the full set of 30-min subsets; results stratified by stability condition are explicitly indicated in the text.

2.9 Error Metrics

To evaluate the performance of TI estimates derived from the lidar using both the traditional and variance methods, two error metrics introduced by DNV are employed: MRBE and RRMSE ~~expressed in percentage~~ (DNV, 2023). The sonic anemometer is used as the reference for all comparisons.

The MRBE quantifies the average relative deviation of the lidar-based estimate X from the sonic-based reference X_{ref}, and is defined as:

$$\mathrm{MRBE} = \frac{1}{N}\sum_{j=1}^{N}\frac{X_j - X_{\mathrm{ref},j}}{X_{\mathrm{ref},j}} \tag{21}$$

The RRMSE reflects the relative magnitude of deviations and is given by:

$$\mathrm{RRMSE} = \sqrt{\frac{1}{N}\sum_{j=1}^{N}\left(\frac{X_j - X_{\mathrm{ref},j}}{X_{\mathrm{ref},j}}\right)^2} \tag{22}$$

Here, X_j denotes ~~the~~ TI estimated from the lidar (either by the traditional or variance method), and $X_{\mathrm{ref},j}$ is the corresponding TI derived from the sonic anemometer, for each of the N 30-min ensembles. These metrics provide complementary insight: MRBE indicates systematic bias (over- or underestimation), while RRMSE captures the overall scatter or consistency of the estimate.

3 Results

3.1 ~~Variances~~

~~The cumulative distribution functions (CDFs) of the along- and cross-wind velocity variances, computed from sonic anemometer measurements and lidar-derived estimates using both methods, are presented in Fig. **??**. The mean along-wind variance measured by the sonic anemometer,~~ ~~σ_u^2~~~~, was found to be 0.721 m^2/s^2. For the along-wind variance,~~ ~~$\tilde{\sigma}_u^2$~~~~, estimated using the traditional method, the mean value was overestimated by 3.5% compared to the reference measurement. In contrast, the variance method yielded an underestimation, with~~ ~~$\hat{\sigma}_u^2$~~ ~~being 5.4% lower than the reference mean (Fig. **??**a). The cross-wind variance showed a more pronounced discrepancy between the two methods. The CDF of~~ ~~$\hat{\sigma}_v^2$~~~~, obtained via the variance method, closely matched that of the reference variance,~~ ~~σ_v^2~~~~, with nearly identical mean values of 0.474 m^2/s^2 and a slight underestimation of 0.4% (Fig. **??**b). In contrast, the traditional method significantly overestimated the cross-wind variance, with~~ ~~$\tilde{\sigma}_v^2$~~ ~~exceeding the reference mean by 33.6%. Cumulative distribution functions of the along-wind velocity variances (a) and cross-wind velocity variances (b), computed from sonic anemometer measurements and lidar-derived estimates using the traditional and variance method. The vertical dashed lines shows the mean variances.~~

~~Slope values from linear regressions between wind variances estimated by each method and reference sonic anemometer measurements, categorized by atmospheric stability conditions. "DL" refers to the dual-lidar configuration using the variance method, and "SL" refers to the single-lidar configuration using the traditional method. Results associated with the 6-beam~~

~~method are reproduced from Sathe et al. (2015). A slope of 1 indicates perfect agreement with the reference.~~ **~~Methods~~** ~~DL SL 6-beam DL SL 6-beam DL SL 6-beam Along-wind variance 0.92 1.02 0.85 0.91 0.94 0.87 0.97 1.02 1.01 Cross-wind variance 0.90 1.21 0.87 0.96 1.06 0.90 0.99 1.32 0.91 To further quantify the differences in variance estimation, we analyzed the slopes of linear regressions between each method's variance estimates and the reference sonic anemometer measurements. As a benchmark, we also include slope results from the 6-beam method reported by Sathe et al. (2015). The results are shown in Fig.~~ **~~??~~** ~~and summarized in Table~~ **~~??~~**~~. For conciseness, scatter plots are omitted; however, since the intercepts were consistently near zero, the slope alone effectively characterizes the proportional agreement. Here, slope values (which are dimensionless and typically close to 1) are expressed as percentages by multiplying by 100 to facilitate interpretation—for example, a slope of 0.92 is presented as 92%, indicating that the method estimates 92% of the reference variance.~~

~~Across all stability regimes, the dual-lidar configuration associated with the variance method consistently estimated between 90% and 97% of the reference variance values for both along- and cross-wind components. Conversely, the single-lidar method associated with the traditional approach generally overestimated variances, particularly the cross-wind component under neutral and unstable conditions, where values reached 132% and 121% of the reference, respectively. Under stable conditions, estimates derived from the traditional approach were closer to the reference, overestimating by 6% or less. The 6-beam method consistently underestimated variance values, with along-wind variances ranging from 85% to 101%, and cross-wind variances from 87% to 91% of the reference, depending on stability. Histograms of the slope values from linear regressions between wind variance estimates and reference sonic anemometer measurements: (a) along-wind variance and (b) cross-wind variance. The comparison includes three methods: the dual-lidar configuration using the variance method, the single-lidar configuration using the traditional method, and the benchmark 6-beam method adapted from Sathe et al. (2015). Dashed areas overlaid on the bars represent the discrepancy between each method's slope and the ideal reference value of 1, which indicates perfect agreement with the reference measurements.~~

3.1 Velocity spectra

Fig. 5 shows the ~~mean~~ premultiplied ensemble-averaged spectra of the along-wind and cross-wind velocity components, ~~averaged under different atmospheric stability conditions~~ obtained as the arithmetic mean of premultiplied 30-min spectra within each atmospheric stability class and compared with reference spectra ~~obtained~~ derived from sonic anemometer measurements. Across all stability regimes and for both ~~components, a consistent pattern emerges:~~ velocity components, the variance method ~~systematically~~ underestimates spectral energy at low frequencies, ~~agrees reasonably well~~ shows reasonable agreement at intermediate frequencies, and ~~flattens at~~ exhibits an increase in spectral energy toward higher frequencies in ~~a manner characteristic of white noise. Overall, however, the mean spectra from the variance method remain largely consistent with the reference spectra.~~

~~In contrast,~~ the premultiplied spectra consistent with white-noise behavior. In the traditional method~~reproduces the reference spectra more accurately at low frequencies.~~, the corresponding white-noise plateau is not observable because the high-frequency portion of the spectra is contaminated by inter-beam effects. These inter-beam contributions distort the spectral shape and mask the underlying noise behavior, preventing the identification of a distinct noise-dominated regime.

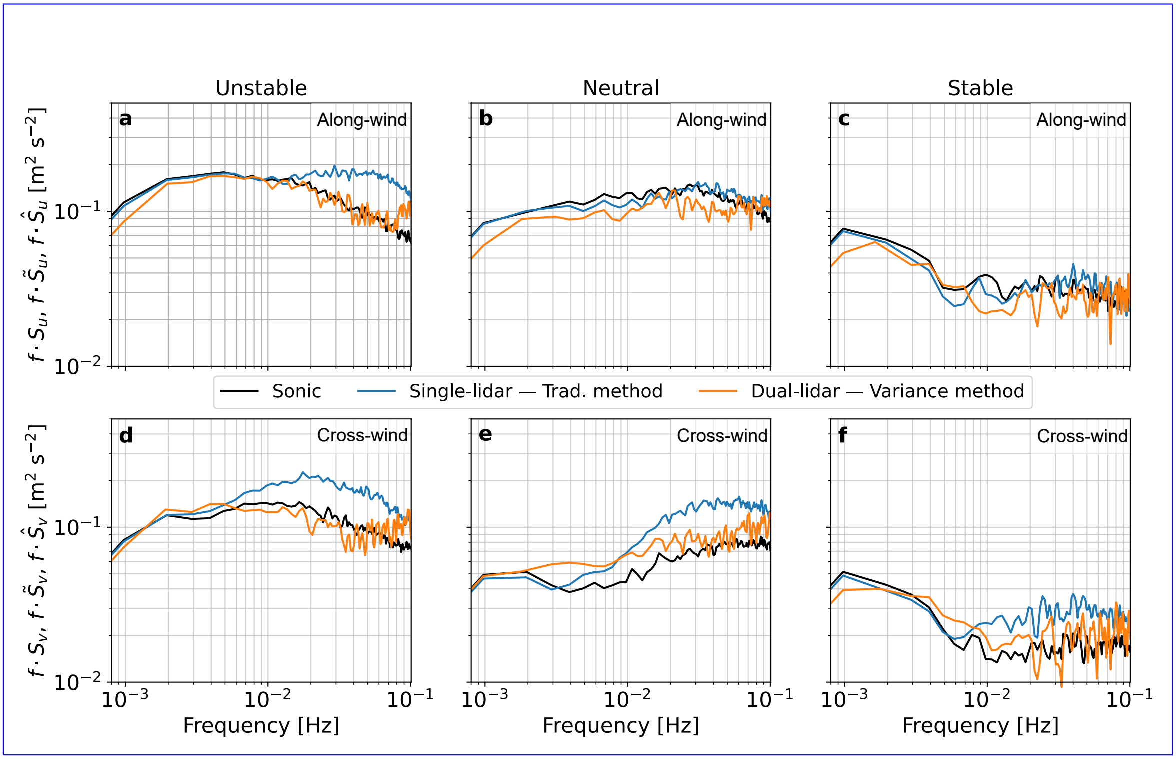

Figure 5. ~~Mean~~ Premultiplied ensemble-averaged spectra of the along-wind and cross-wind velocity components (mean of 30-min premultiplied spectra within each stability class) derived from the traditional and variance ~~method, averaged under different atmospheric stability conditions,~~ methods and compared ~~against reference spectra derived from~~ with sonic anemometer ~~measurements~~reference spectra.

For the traditional method, the agreement with the reference spectra depends on the velocity component and atmospheric stability. For the along-wind component, ~~it matches the reference spectra under neutral and stable conditions (Fig. 5b–c). Under unstable conditions, however, the along-wind spectrum (Fig. 5a), as well as the cross-wind spectra~~ good agreement is observed at low frequencies across all stability ~~regimes (Fig. 5d–f), consistently~~ classes, while under unstable conditions the spectra exceed the reference ~~spectra~~ at intermediate and ~~higher frequencies. This leads to a systematic overestimation of spectral energy and variance~~high frequencies. For the cross-wind component, the traditional method exhibits higher spectral energy than the reference spectra across all stability regimes, particularly at intermediate and high frequencies.

3.2 Turbulence intensity

Fig. 6a-c present scatter plots of the along- and cross-wind TI estimates, $\tilde{\mathrm{TI}}_u$ and $\tilde{\mathrm{TI}}_v$, obtained using the traditional method, plotted against the reference TI values. In contrast, Fig. 6b-d display scatter plots of the along- and cross-wind TI estimates, $\hat{\mathrm{TI}}_u$ and $\hat{\mathrm{TI}}_v$, derived using the variance method also plotted against the reference TI. Linear regression models fitted to each dataset are constrained to pass through the origin (zero intercept). The slopes of these regression lines reveal that the traditional

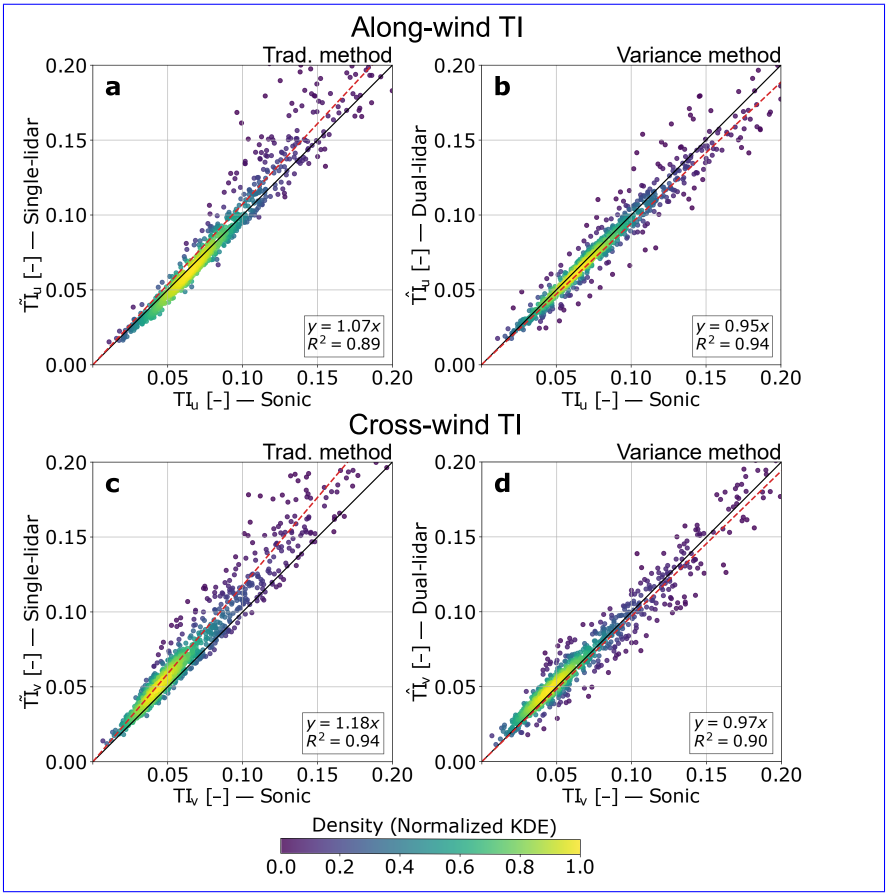

Figure 6. Scatter plots of along- and cross-wind TI estimates obtained using two different methods. Panels (a) and (c) show $\tilde{\mathrm{TI}}_u$ and $\tilde{\mathrm{TI}}_v$, respectively, derived using the traditional method applied to single-lidar measurements. Panels (b) and (d) show $\hat{\mathrm{TI}}_u$ and $\hat{\mathrm{TI}}_v$, respectively, derived using the variance method based on dual-lidar measurements. Red dashed lines indicate linear regression fits, with the corresponding regression equations and R^2 values displayed in the bottom-right corner of each panel. Points are color-coded according to normalized kernel density estimation (KDE).

method systematically overestimates TI, with $\tilde{\mathrm{TI}}_u$ and $\tilde{\mathrm{TI}}_v$ being approximately 107% and 118% of the reference values, respectively. Conversely, the variance method underestimates TI, yielding $\hat{\mathrm{TI}}_u$ and $\hat{\mathrm{TI}}_v$ values that correspond to approximately 95% and 97% of the reference TI. In terms of coefficient of determination (R^2), the variance method demonstrates improved performance for the along-wind component, achieving $\mathrm{R}^2 = 0.94$, compared to $\mathrm{R}^2 =$ ~~0.90~~ 0.89 for the traditional method. However, for the cross-wind component, the traditional method ~~slightly outperforms~~ performs better than the variance method, with $\mathrm{R}^2 = 0.94$ versus $\mathrm{R}^2 = 0.90$. ~~Comparison of mean absolute MRBE and RRMSE for along-wind and cross-wind TI estimates reconstructed using the traditional method (TM) with single-lidar (SL) measurements and the variance method (VM) with dual-lidar (DL) measurements, across different atmospheric stability conditions. The category "All" represents the full dataset without separation by stability class.~~

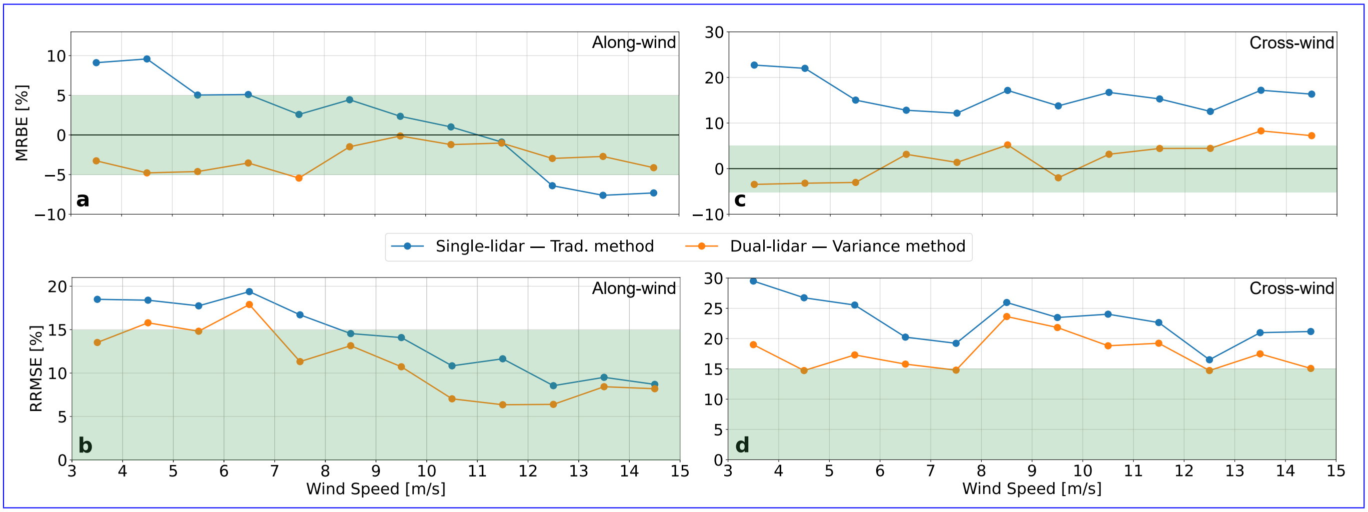

Figure 7. Binned-averaged MRBE (~~a-c~~a,c) and RRMSE (~~b-d~~b,d) of the along-wind and cross-wind TI derived from the traditional and variance methods as a function of binned-averaged wind speed. The green shaded areas indicate the DNV load validation acceptance criteria: MRBE within $\pm$5% and RRMSE $\leq$ 15%. Only bins with sufficient data are shown.

Fig. 7 shows the binned-averaged MRBE and RRMSE of the along-wind and cross-wind TI as a function of binned-averaged wind speed. A key observation is that the error metrics associated with the reconstruction of TI using the variance method are consistently lower than those ~~from~~ obtained with the traditional method across nearly all ~~wind speed bins. There is no clear evidence of a~~ wind-speed bins. No strong dependence of MRBE or RRMSE on wind speed is observed, except for the RRMSE of the along-wind TI (Fig. 7b), which clearly decreases ~~as wind speedincreases. The absolute MRBE for~~ with increasing wind speed. The MRBE for the along-wind TI derived using the variance method remains within ~~the range of 0-5% , while this range nearly doubles (0-10%) for~~ -5% to 0%, while the traditional method yields a considerably wider range of -10% to 10%. For both methods, the error metrics associated with cross-wind TI is approximately 1.5 to 1.8 times higher than ~~the respective error for~~ that of the along-wind ~~TI. Furthermore, the error metrics for the traditional method generally vary over a range nearly twice as wide as those for the variance method.~~ TI.

With respect to DNV load-validation acceptance criteria, the variance method provides TI estimates that satisfy the criteria for both MRBE and RRMSE for the along-wind TI, and for MRBE for the cross-wind TI. However, the acceptance criterion for RRMSE of the cross-wind TI is not met with this method. For the traditional method, the DNV acceptance criteria for both MRBE and RRMSE of the along-wind TI are met only at wind speeds above approximately 7 m/s, while the criteria are not satisfied for the cross-wind TI across the investigated wind-speed range. Fig. 8 shows the mean absolute MRBE and RRMSE for along- and cross-wind TI reconstructed using both methods. The results are summarized in Table 2. The mean absolute MRBE values for along-wind TI indicate that the variance method yields lower errors across all stability regimes. Specifically, in unstable conditions, the MRBE decreases from 10.4% using the traditional method to 7.4% using the variance method. In stable and neutral conditions, the variance method maintains slightly lower MRBE values of 8.1% and 6.3%, compared to 8.3%

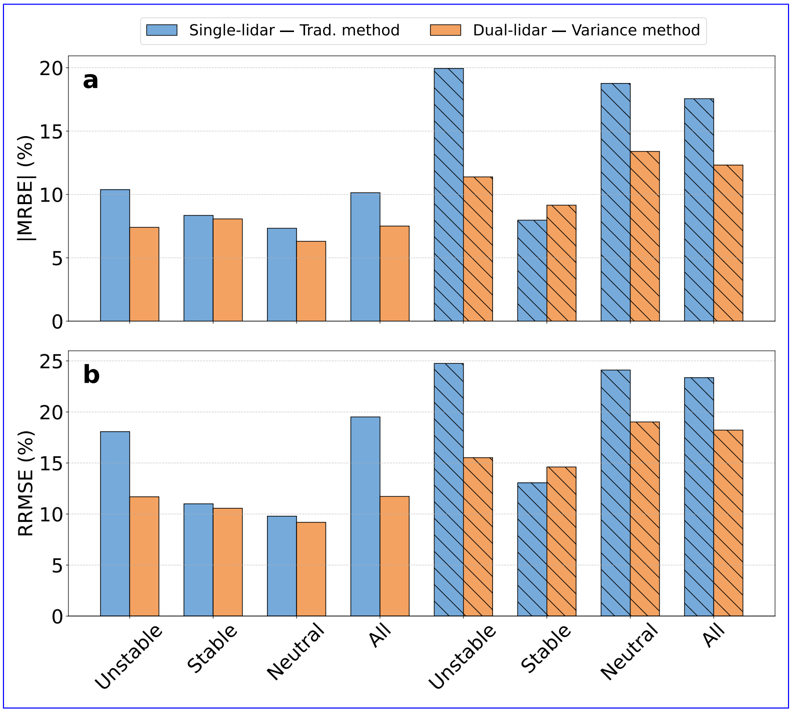

Figure 8. Mean absolute MRBE (a) and RRMSE (b) for along-wind (solid colored bars) and cross-wind (patterned colored bars) TI estimates reconstructed using the traditional method and the variance method across different atmospheric stability conditions. The "All" category represents the entire dataset without differentiation by stability class.

Table 2. Comparison of mean absolute MRBE and RRMSE for along-wind and cross-wind TI estimates reconstructed using the traditional method (TM) with single-lidar (SL) measurements and the variance method (VM) with dual-lidar (DL) measurements, across different atmospheric stability conditions. The category "All" represents the full dataset without separation by stability class.

Conditions	**Unstable**		**Stable**		**Neutral**		**All**	
Methods	SL — TM.	DL — VM.	SL — TM	DL — VM.	SL — TM	DL — VM	SL — TM	DL — VM
|MRBE| (%) — Along-wind TI	10.4	7.4	8.3	8.1	7.3	6.3	10.1	7.5
|MRBE| (%) — Cross-wind TI	20.0	11.4	8.0	9.2	18.8	13.4	17.6	12.3
RRMSE (%) — Along-wind TI	18.1	11.7	11.0	10.6	9.8	9.2	19.5	11.7
RRMSE (%) — Cross-wind TI	24.8	15.5	13.1	14.6	24.1	19.0	23.4	18.2

and 7.3% for the traditional method, respectively. For the entire dataset, the mean absolute MRBE for the variance method is 7.5%, compared to 10.1% for the traditional method. For cross-wind TI, the traditional method yields higher MRBE values under unstable and neutral conditions (20.0% and 18.8%, respectively), while the variance method reduces these errors to 11.4% and 13.4%. Under stable conditions, the traditional method produces a slightly lower MRBE than the variance method

(8.0% versus 9.2%). Considering the full dataset, the mean absolute MRBE decreases from 17.6% with the traditional method to 12.3% with the variance method.

Regarding RRMSE, for along-wind TI, the variance method results in lower errors than the traditional method for all stability regimes. Across the entire dataset, the variance method achieves an RRMSE of 11.7%, whereas the traditional method reports 19.5%. For cross-wind TI, the variance method lowers RRMSE values during unstable and neutral conditions but produces a slightly higher error under stable conditions. Across the full dataset, however, the variance method achieves a lower overall RRMSE of 18.2% compared to 23.4% for the traditional method.

4 Discussion

The ~~ability~~ capability of the variance method applied in a dual-lidar configuration to ~~measure turbulence was compared against both the traditional approach employed~~ quantify turbulence was evaluated against the conventional approach commonly used in the wind power industry~~and the 6-beam method, with results from the latter taken from Sathe et al. (2015). Since the 6-beam method was evaluated using a completely different dataset, it is not possible to identify a single best method for turbulence estimation. Instead, the goal here is to provide an order-of-magnitude comparison and highlight possible improvements.~~

~~As with the variance method,~~ . Overall, relative to the ~~6-beam approach is affected only by intra-beam effect. Although the authors did not explicitly remove instrumental noise, its contribution was considered negligible. The 6-beam method relies on measurements from the WindScanner, which incorporates the scanning pulsed lidar WindCube 200 by Vaisala (Vasiljević et al., 2016). This device features an extended probe length of about 100 m, in contrast to pulsed lidar profilers. Since noise levels decrease with increasing probe volume, the WindScanner measurements are therefore expected to be largely unaffected by noise. In general, smaller probe volumes produce higher noise because fewer scatterers contribute to the backscattered signal, which reduces the signal strength relative to the detector's noise floor. Consequently, the signal-to-noise ratio decreases, resulting in higher instrumental noise in the retrieved measurements.~~

~~Overall, the 6-beam method produced lower variances compared to the variance method applied on the dual-lidar configuration, which itself tends to underestimate turbulence metrics.~~ reference instrument, an underestimation of turbulent energy was observed, as evidenced by both TI and the velocity spectra. This discrepancy is most likely attributable to ~~the WindScanner's lower sampling rate~~probe-time averaging inherent to pulsed Doppler lidar measurements, which is ~~nearly four times smaller than that of the WindCube v2.1. The sampling rate is governed~~ governed primarily by the accumulation time, Δt, ~~which enters the transfer function, H, applied by the instrument to the measured signal (Thiébaut et al., 2025):~~

$$|H|^2(\mathbf{k}) = \mathrm{sinc}^2\left(\frac{\Delta t}{2}\mathbf{k}\cdot\mathbf{U}\right)\exp\left(-\left[\sigma_l^2(\mathbf{k}\cdot\mathbf{b})^2 + \sigma_r^2(\parallel\mathbf{k}\parallel^2 - (\mathbf{k}\cdot\mathbf{b})^2)\right]\right)$$

~~Here, **k** is the turbulent structure wavevector, **b** is the beam pointing vector, **U** is the wind velocity vector of magnitude U, and σ_l~~ and ~~σ_r represent Gaussian weighting factors in the along-beam and cross-beam directions, respectively. From Eq. **??**, it follows that wind fieldstructures with wavelengths smaller than σ_l in the along-beam direction are attenuated, as are those~~

~~with wavelengths smaller than σ_r in the cross-beam direction. However, in the latter case, these structures are so small that the filtering effect becomes negligible, since the probe cross-section is approximately 1 cm (Thiébaut et al., 2025). Assuming the Taylor frozen turbulence hypothesis, the wavevector domain transmitted by the filter is defined by the intersection of two slices: one perpendicular to $\mathbf{U}$, which preserves structures longer than $\pi \Delta t U$, and another perpendicular to $\mathbf{b}$, which retains structures longer than σ_l. All other structures are filtered out.~~

the effective probe length. Both effects introduce temporal and spatial averaging of the wind field, thereby filtering out turbulent fluctuations with scales smaller than the probe volume. To preserve smaller ~~structures, Δt~~ turbulent structures, the accumulation time must be reduced~~, thereby increasing the sampling rate. Thiébaut et al. (2025) demonstrated that raising the sampling rate from~~. Thiébaut et al. (2025) demonstrated that decreasing the accumulation time at each LOS position from 0.8 s—corresponding to a sampling rate of 0.25~~Hz (commercial lidar) to~~ Hz in standard commercial lidar configurations—to 0.2 s, corresponding to a 1~~Hz~~ Hz sampling rate for the WindCube v2.1, increases the along-wind variance ~~derived~~ obtained from the variance method by ~~about~~ approximately 7%~~compared with the commercial sampling rate~~, without significantly reducing data availability (a ~~loss~~ decrease of 0.5%). ~~A target sampling rate of 1 Hz for future lidar profilers may therefore represent a good trade-off between data availability and turbulence resolution.~~

~~The 6-beam method forms the basis of the pulsed Beam6X WindPower lidar profiler developed by Lumibird, which combines five slanted beams with one vertical beam. The variance method described in this paper can be applied to this technology using a single lidar. However, a full measurement cycle over the six beams of the Beam6X WindPower requires approximately 6 s, corresponding to a sampling rate of 0.167 Hz—only 33% of that of the commercial WindCube v2.1 and 83% lower than the targeted 1 Hz. Consequently, the turbulence measurement performance of the Beam6X WindPower is currently expected to be comparable to that of~~ Building on the well-known impact of probe-volume averaging, Manami et al. (2025) proposed a method to recover part of the filtered turbulent energy by exploiting Doppler spectral information rather than relying solely on LOS velocities. Their results indicate that a larger fraction of the turbulence statistics can be retrieved when spectral broadening effects are taken into account. In this context, the ~~WindScanner. Reducing the accumulation time and thus increasing the sampling rate will likely be necessary to match the performance of the dual-lidar configuration with two WindCube v2.1 systems. Nevertheless, the clear advantage of the Beam6X WindPower is that the variance method becomes applicable in all wind directions with a single lidar.~~

~~The variance method can be applied with the continuous-wave ZX300 lidar profiler. The ZX300 records about 50 LOS positions per second, corresponding to an accumulation time of 20 ms per LOS, which increases measurement noise. These LOS positions are distributed azimuthally along a circle at a fixed elevation angle. A further drawback is that a full scan at one altitude requires 1 s, meaning that the effective sampling rate decreases with the number of altitudes measured. To reach a 1 Hz sampling rate, the device must therefore be restricted to a single altitude, most likely the hub height of wind turbines. To reproduce the 0.25 Hz sampling rate of the commercial WindCube v2.1, measurements could be taken at a maximum of four altitudes. Despite these constraints, the ZX300 offers the advantage of a shorter probe length that increases with altitude (e.g., 7.7 m at 100 m above ground level), compared to the WindCube v2.1, which has a constant probe length of 23 m (Thiébaut et al., 2025). The shorter probe length has the potential to reduce intra-beam averaging errors and thereby~~

~~improve the accuracy of turbulence estimates~~systematic underestimation of turbulent energy observed in the present study can be interpreted as a direct consequence of conventional velocity-based retrieval techniques, which remain intrinsically affected by probe-volume averaging. The comparison therefore highlights both the fundamental limitations imposed by probe length and accumulation time and the potential of advanced spectral-based approaches for improving turbulence characterization with pulsed Doppler lidars.

The variance method ~~produces~~ yields lower mean MRBE and RRMSE ~~for all stability conditions~~ across all stability regimes except for the cross-wind TI ~~during~~ under stable conditions. ~~During these conditions, turbulence is generally weak and dominated by larger, more coherent eddies. In this regime, the assumption of spatial homogeneity is more likely to hold, so~~ Under stable stratification, TI is generally low and often dominated by small-scale fluctuations, which limits the overall turbulent energy available. In such cases, the reduced energy content can diminish the magnitude of inter-beam ~~contamination is limited and the traditional method tends to yield smaller errorsin TI reconstruction. In contrast, under unstable or neutral~~ effects in the traditional reconstruction, leading to smaller errors. Under neutral and unstable conditions, turbulence is ~~stronger, more intermittent,~~ typically stronger and characterized by a broader range of ~~eddy sizes. Violations of the homogeneity assumption become more pronounced, enhancing~~ energetic scales, which increases the sensitivity of inter-beam ~~contamination~~ reconstruction methods to spatial separation between beams. While intermittent turbulence and violations of homogeneity can also occur under stable conditions—particularly in the presence of strong shear—the higher overall turbulence levels commonly observed under neutral and unstable stratification tend to amplify inter-beam effects in the traditional method. ~~As~~ Because the variance method ~~is not subject to inter-beam effects and~~ relies directly on LOS velocity statistics and avoids inter-beam reconstruction, it provides more reliable estimates of TI ~~in unstable and neutral regimes~~under these conditions, despite remaining sensitive to intra-beam averaging.

The corresponding spectral differences reflect the distinct sampling and reconstruction mechanisms of the two approaches. At low frequencies, the traditional method captures large-scale, slowly evolving motions that remain coherent over the scan volume, leading to good agreement with the reference sonic measurements. In contrast, spectra derived from the variance method show a systematic underestimation of energy in the low-frequency range. This behaviour does not arise from direct spatial filtering by the finite probe length, which primarily affects small-scale fluctuations, but from the nature of the variance method itself. Large-scale turbulent motions are nearly uniform across the lidar probe volume and therefore mainly affect the mean line-of-sight velocity, while producing little variability within the probe. Because the variance method relies on velocity fluctuations within the sampling volume rather than on the absolute velocity, these coherent motions contribute less energy to the reconstructed spectrum than they do in point measurements from the sonic anemometer.

At intermediate frequencies, where turbulent fluctuations become increasingly decorrelated across the probe volume, spectra derived from the variance method show good agreement with those obtained from the sonic anemometer. At higher frequencies, however, spectra from the variance method depart from the sonic reference and exhibit a white-noise behaviour, reflecting the growing influence of instrumental noise and the limited sensitivity of the method at small scales. At high frequencies, the traditional method modifies the reconstructed spectrum through a wavenumber-dependent response associated with beam separation, as a consequence of the inter-beam ~~effect, inherent only to the traditional method, is the most unpredictable because~~

~~it depends strongly~~ effect, which can artificially enhance small-scale energy (Kelberlau et al., 2020). This effect is strongest under neutral and unstable conditions, where the inertial subrange is well developed, and is reduced under stable conditions, where high-wavenumber turbulence is suppressed.

The magnitude of inter-beam effects further depends on local site characteristics. ~~Physically, this effect arises~~ These effects arise when different beams ~~of the scanning pattern probe air volumes~~ probe flow regions that are not dynamically coherent~~. For example, in complex terrain the airflow may accelerate over a ridge or decelerate in a sheltered valley. Beams sampling these distinct regions can therefore register artificially large velocity differences that do~~ , for example due to mean-flow acceleration over terrain features, sheltering effects, or localized shear and recirculation induced by surface roughness or obstacles. When such spatial gradients are present, sequential sampling of different flow regions combined with advection can map stationary spatial variability onto temporal fluctuations, introducing apparent variance when the beams are combined. This spurious variability does not reflect true turbulence but rather ~~systematic spatial gradients in the mean flow. Similarly, surface roughness or obstacles (e.g., trees, buildings) can generate localized shear layers and recirculation zones, adding spurious high-frequency variability to some beams while leaving others unaffected. Such effects~~ space–time sampling effects, and it can either amplify or attenuate the apparent turbulent energy~~when the beams are combined, making error metrics highly site-specific and difficult to generalize~~. As a result, the performance of the traditional method can be strongly site-dependent, whereas the variance method is less sensitive to such effects.

In contrast, the variance method is impacted primarily by the intra-beam effect, which is systematic and thus more predictable. This makes the variance method potentially more robust and transferable across different sites. Furthermore, TI derived from the variance method exhibited smaller variations across the stability regimes examined, suggesting that atmospheric stratification has a weaker influence on its ability to capture the underlying turbulence level compared to the traditional method.

For both methods, a marked difference was observed between the along-wind and cross-wind TI, with significantly larger errors associated with the latter. Nevertheless, the variance method consistently yielded lower errors than the traditional approach. ~~This difference is mainly due to the rotation from instrument coordinates to along- and cross-wind coordinates: the along-wind component is relatively robust to small directional uncertainties, while the cross-wind component is much more sensitive. Even small errors in the estimated wind direction can lead to disproportionately large errors in the cross-wind variance. In addition, because turbulence energy is generally higher in the along-wind than in the cross-wind direction,~~ Velocity reconstruction relies on LOS measurements acquired at different times, and the ~~relative impact of these directional errors becomes more pronounced for the latter. Together, these factors explain why the along-wind variance is typically well captured, whereas the~~ associated temporal decorrelation affects the velocity components differently. Along-wind fluctuations, which are advected by the mean flow, remain correlated over the scan cycle, whereas cross-wind ~~variance remains more uncertain.~~

~~This imbalance between the along- and cross-wind variances is not only a methodological concern but also has practical implications for wind turbine load assessment. The along-wind component dominates TI and is directly linked to variations in power production, as well as to fatigue and ultimate loads on the rotor blades and tower. In contrast, the cross-wind component plays a critical role in generating yaw and lateral tower loads, and in inducing asymmetric blade loading. Despite the higher uncertainty in cross-wind variance, the variance method still outperforms the traditional method in capturing~~

~~this component, reducing measurement errors and improving overall turbulence characterization. Although its variance is typically smaller, underestimating the cross-wind turbulence leads to a systematic bias in the predicted lateral excitation of the turbine.~~ fluctuations decorrelate more rapidly (Sathe and Mann, 2012). As a result, ~~the use of the variance method without accounting for this limitation may yield non-conservative estimates of turbine loads, especially for large rotors where yaw misalignment and lateral inflow fluctuations are increasingly significant~~combining temporally separated LOS measurements can lead to a reduced or distorted estimate of cross-wind turbulent energy. The variance method mitigates this limitation by avoiding inter-beam reconstruction, although the underlying decorrelation remains intrinsic to sequential scanning. A fully simultaneous multi-beam lidar configuration, analogous to an ADCP, would remove this source of decorrelation and is therefore expected to improve cross-wind turbulence estimates. However, achieving true simultaneity would require multiple independent transmit–receive channels operating at different beam angles, rather than a single laser sequentially steered by a scanner. This would substantially increase optical, electronic, and calibration complexity, and consequently the overall system cost.

5 Conclusions

The variance method applied in a dual-lidar configuration demonstrates improved performance compared to the traditional method in terms of MRBE and RRMSE for both along- and cross-wind TI. Because it is primarily affected by the intra-beam effect, which is systematic and ~~predictable~~physically interpretable, the variance method is largely site-independent and broadly applicable, thereby overcoming the main limitation of the traditional method associated with unpredictable inter-beam errors. Moreover, turbulence estimates derived from the variance method remain consistent across varying atmospheric stability conditions, highlighting its resilience to stratification effects. Taken together, these features indicate that the dual-lidar approach is now sufficiently mature for validation and practical deployment in ground-based wind measurements, albeit at the expense of increased instrumentation costs associated with the use of two lidar systems.

Cross-wind turbulence exhibits higher ~~relative~~ uncertainty than along-wind turbulence ~~because of its sensitivity to wind direction estimation. Nonetheless,~~ due to temporal decorrelation associated with sequential LOS sampling. While the variance method ~~captures the overall turbulence characteristics accurately. This distinction has practical relevance: along-wind turbulence , which dominates power production and rotor fatigue, is well resolved, while the cross-wind component, though smaller, remains adequately represented to inform assessments of lateral loading~~reduces the resulting errors compared with the traditional approach, this limitation remains intrinsic to scanning Doppler lidars. Along-wind turbulence is less affected by this decorrelation, as its dominant fluctuations tend to remain coherent over the scan cycle, which is consistent with the lower uncertainties observed in the along-wind component.

Further improvements in lidar technology and scanning strategies can enhance the performance of the variance method. ~~Its main limitations with current profilersare the short accumulation time per LOS and the reduced effective sampling rate when scanning multiple altitudes.~~ With current profilers, performance is influenced by the accumulation time and probe length, which must be balanced to maintain adequate data availability while preserving sensitivity to turbulent fluctuations.

While the variance method avoids inter-beam reconstruction, temporal decorrelation associated with sequential scanning remains intrinsic to current systems, particularly affecting cross-wind turbulence estimates. Fully simultaneous multi-beam lidar configurations could alleviate this limitation, but at the cost of substantially increased system complexity and expense. Nevertheless, the variance method remains a promising and versatile approach for accurate, site-independent turbulence measurements, supporting reliable wind energy assessments and load modeling.

Author contributions

MT identified the ~~problematic~~problem, performed the analysis, and drafted the paper. NL reviewed the manuscript.

Data availability

The high-frequency velocity data from the dual-lidar and sonic anemometer measurements used in this study are provided alongside this paper. To comply with confidentiality agreements, all velocity components have been multiplied by an undisclosed constant scaling factor. This transformation preserves all relative variations, turbulence characteristics, and statistical relationships among instruments.

Acknowledgments

We would like to thank Vaisala for providing the secondary lidar, which enabled the implementation of the dual-lidar configuration and made this study possible.

Competiting interest

The authors declare that they have no conflict of interest.

Financial support

This work was made possible through the support of France Energies Marines and the French government, managed by the Agence Nationale de la Recherche under the Investissements d'Avenir program, with the reference ANR-10-IEED-0006-34. This work was carried out in the framework of the DRACCAR-NEMO project.

References

Bodini, N., Lundquist, J. K., and Newsom, R. K.: Estimation of turbulence dissipation rate and its variability from sonic anemometer and wind Doppler lidar during the XPIA field campaign, Atmospheric Measurement Techniques, 11, 4291–4308, https://doi.org/10.5194/amt-11-4291-2018, 2018.

Browning, K. A. and Wexler, R.: The determination of kinematic properties of a wind field using Doppler radar, Journal of Applied meteorology and climatology, 7, 105–113, https://doi.org/10.1175/1520-0450(1968)007<0105:tdokpo>2.0.co;2, 1968.

Brugger, P., Träumner, K., and Jung, C.: Evaluation of a procedure to correct spatial averaging in turbulence statistics from a Doppler lidar by comparing time series with an ultrasonic anemometer, Journal of Atmospheric and Oceanic Technology, 33, 2135–2144, https://doi.org/10.1175/jtech-d-15-0136.1, 2016.

Burchard, H., Craig, P. D., Gemmrich, J. R., van Haren, H., Mathieu, P.-P., Meier, H. M., Smith, W. A. M. N., Prandke, H., Rippeth, T. P., and Skyllingstad, E. D.: Observational and numerical modeling methods for quantifying coastal ocean turbulence and mixing, Progress in oceanography, 76, 399–442, https://doi.org/10.1016/j.pocean.2007.09.005, 2008.

DNV: Lidar-measured turbulence intensity for wind turbines, Tech. Rep. DNV-RP-0661, https://www.dnv.com/energy/standards-guidelines/dnv-rp-0661-lidar-measured-turbulence-intensity-for-wind-turbines/, 2023.

Doviak, R. J. and Zrnic, D. S.: Doppler Radar & Weather Observations, Courier Corporation, https://doi.org/10.1016/c2009-0-22358-0, 1993.

Durgesh, V., Thomson, J., Richmond, M. C., and Polagye, B. L.: Noise correction of turbulent spectra obtained from acoustic doppler velocimeters, Flow Measurement and Instrumentation, 37, 29–41, https://doi.org/10.1016/j.flowmeasinst.2014.03.001, 2014.

Eberhard, W. L., Cupp, R. E., and Healy, K. R.: Doppler lidar measurement of profiles of turbulence and momentum flux, Journal of Atmospheric and Oceanic Technology, 6, 809–819, https://doi.org/10.1175/1520-0426(1989)006<0809:dlmopo>2.0.co;2, 1989.

Foken, T. and Mauder, M.: Micrometeorology, Springer Atmospheric Sciences, https://doi.org/10.1007/978-3-031-47526-9, 2008.

Garbini, J. L., Forster, F. K., and Jorgensen, J. E.: Measurement of fluid turbulence based on pulsed ultrasound techniques. Part 2. Experimental investigation, Journal of Fluid Mechanics, 118, 471–505, https://doi.org/10.1017/s0022112082001165, 1982.

Gargett, A. E., Tejada-Martinez, A. E., and Grosch, C. E.: Measuring turbulent large-eddy structures with an ADCP. Part 2. Horizontal velocity variance, https://doi.org/10.1357/002224009791218823, 2009.

Goddijn-Murphy, L., Woolf, D. K., and Easton, M. C.: Current patterns in the inner sound (Pentland Firth) from underway ADCP data*, Journal of Atmospheric and Oceanic Technology, 30, 96–111, https://doi.org/10.1175/jtech-d-11-00223.1, 2013.

Hurther, D. and Lemmin, U.: A correction method for turbulence measurements with a 3D acoustic Doppler velocity profiler, Journal of Atmospheric and Oceanic Technology, 18, 446–458, https://doi.org/10.1175/1520-0426(2001)018<0446:acmftm>2.0.co;2, 2001.

Kaimal, J. C. and Finnigan, J. J.: Atmospheric boundary layer flows: their structure and measurement, Oxford university press, https://doi.org/10.1093/oso/9780195062397.001.0001, 1994.

Kelberlau, F. and Mann, J.: Better turbulence spectra from velocity–azimuth display scanning wind lidar, Atmospheric Measurement Techniques, 12, 1871–1888, https://doi.org/10.5194/amt-12-1871-2019, 2019.

Kelberlau, F. and Mann, J.: Cross-contamination effect on turbulence spectra from Doppler beam swinging wind lidar, Wind Energy Science, 5, 519–541, https://doi.org/10.5194/wes-5-519-2020, 2020.

Kelberlau, F., Neshaug, V., Lønseth, L., Bracchi, T., and Mann, J.: Taking the motion out of floating lidar: Turbulence intensity estimates with a continuous-wave wind lidar, Remote Sensing, 12, 898, 2020.

Lenschow, D. H., Mann, J., and Kristensen, L.: How long is long enough when measuring fluxes and other turbulence statistics?, Journal of Atmospheric and Oceanic Technology, 11, 661–673, https://doi.org/10.1175/1520-0426(1994)011<0661:hlilew>2.0.co;2, 1994.

Lenschow, D. H., Wulfmeyer, V., and Senff, C.: Measuring second-through fourth-order moments in noisy data, Journal of Atmospheric and Oceanic technology, 17, 1330–1347, https://doi.org/10.1175/1520-0426(2000)017<1330:mstfom>2.0.co;2, 2000.

Lhermitte, R. and Lemmin, U.: Open-channel flow and turbulence measurement by high-resolution Doppler sonar, Journal of atmospheric and oceanic technology, 11, 1295–1308, https://doi.org/10.1175/1520-0426(1994)011<1295:ocfatm>2.0.co;2, 1994.

Lu, Y. and Lueck, R. G.: Using a broadband ADCP in a tidal channel. Part I: Mean flow and shear, Journal of Atmospheric and Oceanic Technology, 16, 1556–1567, 1999.

Lueck, R. G., Wolk, F., and Yamazaki, H.: Oceanic velocity microstructure measurements in the 20th century, Journal of Oceanography, 58, 153–174, https://doi.org/10.1023/a:1015837020019, 2002.

Manami, M., Mann, J., Sjöholm, M., Léa, G., and Gorju, G.: Squeezing turbulence statistics out of a pulsed Doppler lidar, Atmospheric Measurement Techniques, 18, 7513–7523, https://doi.org/10.5194/amt-18-7513-2025, 2025.

Mann, J., Peña, A., Bingöl, F., Wagner, R., and Courtney, M. S.: Lidar scanning of momentum flux in and above the atmospheric surface layer, Journal of Atmospheric and Oceanic Technology, 27, 959–976, https://doi.org/10.1175/2010jtecha1389.1, 2010.

Mayor, S. D., Lenschow, D. H., Schwiesow, R. L., Mann, J., Frush, C. L., and Simon, M. K.: Validation of NCAR 10.6-micrometer CO 2 Doppler lidar radial velocity measurements and comparison with a 915-MHz profiler, Journal of Atmospheric and Oceanic Technology, 14, 1110–1126, https://doi.org/10.1175/1520-0426(1997)014<1110:vonmcd>2.0.co;2, 1997.

McMillan, J. M., Hay, A. E., Lueck, R. G., and Wolk, F.: Rates of dissipation of turbulent kinetic energy in a high Reynolds number tidal channel, Journal of Atmospheric and Oceanic Technology, 33, 817–837, https://doi.org/10.1175/jtech-d-15-0167.1, 2016.

Mercier, P., Thiébaut, M., Guillou, S., Maisondieu, C., Poizot, E., Pieterse, A., Thiébot, J., Filipot, J.-F., and Grondeau, M.: Turbulence measurements: An assessment of Acoustic Doppler Current Profiler accuracy in rough environment, Ocean Engineering, 226, 108 819, https://doi.org/10.1016/j.oceaneng.2021.108819, 2021.

Peters, H. and Johns, W. E.: Bottom layer turbulence in the Red Sea outflow plume, Journal of physical oceanography, 36, 1763–1785, https://doi.org/10.1175/jpo2939.1, 2006.

Päschke, E. and Detring, C.: Noise filtering options for conically scanning Doppler lidar measurements with low pulse accumulation, Atmospheric Measurement Techniques, 17, 3187–3217, https://doi.org/10.5194/amt-17-3187-2024, 2024.

Rippeth, T. P., Williams, E., and Simpson, J. H.: Reynolds stress and turbulent energy production in a tidal channel, Journal of Physical Oceanography, 32, 1242–1251, https://doi.org/10.1175/1520-0485(2002)032<1242:rsatep>2.0.co;2, 2002.

Sathe, A. and Mann, J.: Measurement of turbulence spectra using scanning pulsed wind lidars, Journal of Geophysical Research: Atmospheres, 117, 2012.

Sathe, A., Gryning, S., and Peña, A.: Comparison of the atmospheric stability and wind profiles at two wind farm sites over a long marine fetch in the North Sea, Wind Energy, 14, 767–780, https://doi.org/10.1002/we.456, 2011.

Sathe, A., Mann, J., Vasiljevic, N., and Lea, G.: A six-beam method to measure turbulence statistics using ground-based wind lidars, Atmospheric Measurement Techniques, 8, 729–740, https://doi.org/10.5194/amt-8-729-2015, 2015.

Sentchev, A., Thiébaut, M., and Schmitt, F. G.: Impact of turbulence on power production by a free-stream tidal turbine in real sea conditions, Renewable Energy, 147, 1932–1940, https://doi.org/10.1016/j.renene.2019.09.136, 2019.

Smalikho, I. N. and Banakh, V. A.: Measurements of wind turbulence parameters by a conically scanning coherent Doppler lidar in the atmospheric boundary layer, Atmospheric Measurement Techniques, 10, 4191–4208, https://doi.org/10.5194/amt-10-4191-2017, 2017.

Stacey, M. T., Monismith, S. G., and Burau, J. R.: Observations of turbulence in a partially stratified estuary, Journal of Physical Oceanography, 29, 1950–1970, https://doi.org/10.1175/1520-0485(1999)029<1950:ootiap>2.0.co;2, 1999a.

Stacey, M. T., Monismith, S. G., and Burau, J. R.: Measurements of Reynolds stress profiles in unstratified tidal flow, Journal of Geophysical Research, 104, 10 935–10 949, https://doi.org/10.1029/1998jc900095, 1999b.

Strauch, R. G., Merritt, D. A., Moran, K. P., Earnshaw, K. B., and De Kamp, D. V.: The Colorado wind-profiling network, Journal of Atmospheric and Oceanic Technology, 1, 37–49, https://doi.org/10.1175/1520-0426(1984)001<0037:tcwpn>2.0.co;2, 1984.

Theriault, K.: Incoherent multibeam Doppler current profiler performance: Part II–Spatial response, IEEE journal of oceanic engineering, 11, 16–25, https://doi.org/10.1109/joe.1986.1145135, 1986.

Thiébaut, M., Sentchev, A., and Bailly du Bois, P.: Merging velocity measurements and modeling to improve understanding of tidal stream resource in Alderney Race, Energy, 178, 460–470, https://doi.org/10.1016/j.energy.2019.04.171, 2019.

Thiébaut, M., Filipot, J.-F., Maisondieu, C., Damblans, G., Duarte, R., Droniou, E., and Guillou, S.: Assessing the turbulent kinetic energy budget in an energetic tidal flow from measurements of coupled ADCPs, Philosophical Transactions of the Royal Society A, 378, 20190 496, https://doi.org/https://doi.org/10.1098/rsta.2019.0496, 2020.

Thiébaut, M., Quillien, N., Maison, A., Gaborieau, H., Ruiz, N., MacKenzie, S., Connor, G., and Filipot, J.-F.: Investigating the flow dynamics and turbulence at a tidal-stream energy site in a highly energetic estuary, Renewable Energy, 195, 252–262, https://doi.org/10.1016/j.renene.2022.06.020, 2022.

Thiébaut, M., Vonta, L., Benzo, C., and Guinot, F.: Characterization of the offshore wind dynamics for wind energy production in the Gulf of Lion, Western Mediterranean Sea, Wind Energy and Engineering Research, 1, 100 002, https://doi.org/10.1016/j.weer.2024.100002, 2024.

Thiébaut, M., Marié, L., Delbos, F., and Guinot, F.: Evaluating the enhanced sampling rate for turbulence measurement with a wind lidar profiler, Wind Energy Science, 10, 1869–1885, https://doi.org/10.5194/wes-10-1869-2025, 2025.

Thomson, J., Polagye, B., Durgesh, V., and Richmond, M. C.: Measurements of turbulence at two tidal energy sites in Puget Sound, WA, Oceanic Engineering, IEEE Journal of Oceanic Engineering, 37, 363–374, https://doi.org/10.1109/joe.2012.2191656, 2012.

Vasiljević, N., Lea, G., Courtney, M., Cariou, J.-P., Mann, J., and Mikkelsen, T.: Long-range WindScanner system, Remote Sensing, 8, 896, https://doi.org/10.3390/rs8110896, 2016.

Vermeulen, B., Hoitink, A. J. F., and Sassi, M. G.: Coupled ADCPs can yield complete Reynolds stress tensor profiles in geophysical surface flows, Geophysical Research Letters, 38, https://doi.org/10.1029/2011gl046684, 2011.

Wang, H., Barthelmie, R. J., Clifton, A., and Pryor, S. C.: Wind measurements from arc scans with Doppler wind lidar, Journal of Atmospheric and Oceanic Technology, 32, 2024–2040, https://doi.org/10.1175/jtech-d-14-00059.1, 2015.

Welch, P.: The use of fast Fourier transform for the estimation of power spectra: A method based on time averaging over short, modified periodograms, IEEE Transactions on audio and electroacoustics, 15, 70–73, https://doi.org/10.1109/tau.1967.1161901, 1967.

Wildmann, N., Päschke, E., Roiger, A., and Mallaun, C.: Towards improved turbulence estimation with Doppler wind lidar velocity-azimuth display (VAD) scans, Atmospheric Measurement Techniques, 13, 4141–4158, https://doi.org/10.5194/amt-13-4141-2020, 2020.

Zedel, L., Hay, A. E., Cabrera, R., and Lohrmann, A.: Performance of a single-beam pulse-to-pulse coherent Doppler profiler, IEEE Journal of Oceanic Engineering, 21, 290–297, https://doi.org/10.1109/48.508159, 2002.